UC Berkeley

UC Berkeley Previously Published Works

Title

Ploidy and neuron size impact nervous system development and function in Xenopus

Permalink

https://escholarship.org/uc/item/2kx9j213

Journal

Cell Reports, 45(2)

ISSN

2639-1856

Authors

Liu, Xiao

Wan, Christine

Shah, Sara Aijaz

et al.

Publication Date

2026-02-01

DOI

10.1016/j.celrep.2026.116969

Copyright Information

This work is made available under the terms of a Creative Commons Attribution License, available at https://creativecommons.org/licenses/by/4.0/

Peer reviewed

eScholarship.org Powered by the California Digital Library
University of California

Author Manuscript

Author Manuscript

Author Manuscript

Author Manuscript

HHS Public Access

Author manuscript

Cell Rep. Author manuscript; available in PMC 2026 April 29.

Published in final edited form as:

Cell Rep. 2026 February 24; 45(2): 116969. doi:10.1016/j.celrep.2026.116969.

Ploidy and neuron size impact nervous system development and function in *Xenopus*

Xiao Liu[1,3,*], **Christine Wan**[1], **Sara Aijaz Shah**[1], **Rebecca Heald**[1,2,*]

[1] Department of Molecular and Cell Biology, University of California, Berkeley, Berkeley, CA 94720, USA

[2] Senior author

[3] Lead contact

SUMMARY

Neuron size varies significantly over evolution, contributing to diverse nervous systems of variable complexity, while aberrant neuron size is associated with neurodevelopmental and degenerative diseases. How do neuron cell body and neurite size and organization impact nervous system development and function? To systematically study the effects of neuron size on the vertebrate nervous system, we characterized triploid *Xenopus* tadpoles, which possess a 1.5-fold increase in genome size compared with diploids. Triploid neurons displayed a scaling increase in total volume and a superscaling increase in membrane surface area. Imaging, flow cytometry, and RNA sequencing analyses revealed that triploid brains were morphologically and transcriptionally similar to diploid brains but less proliferative, containing fewer neurons and displaying increased global activity. Interestingly, physiological differences at the neuron and nervous system levels affected swimming behavior in tadpoles. Our findings thus establish a framework to link genome size, neuron size, and nervous system development and function in vertebrates.

In brief

Liu et al. use triploid *Xenopus* as a model to characterize effects of neuron size on vertebrate nervous system development and function. They report association between neuron size, cell proliferation, brain activity, and tadpole swimming behavior.

Graphical Abstract

This is an open access article under the CC BY license (http://creativecommons.org/licenses/by/4.0/).

*Correspondence: xiao.liu@berkeley.edu (X.L.), bheald@berkeley.edu (R.H.).

AUTHOR CONTRIBUTIONS

Conceptualization, X.L. and R.H.; methodology, X.L.; investigation, X.L., C.W., and S.A.S.; data curation, X.L., C.W., and S.A.S.; formal analysis, X.L.; visualization, X.L.; writing – original draft, X.L.; writing – review & editing, X.L. and R.H.; project administration, X.L.; funding acquisition, R.H.; supervision, R.H.

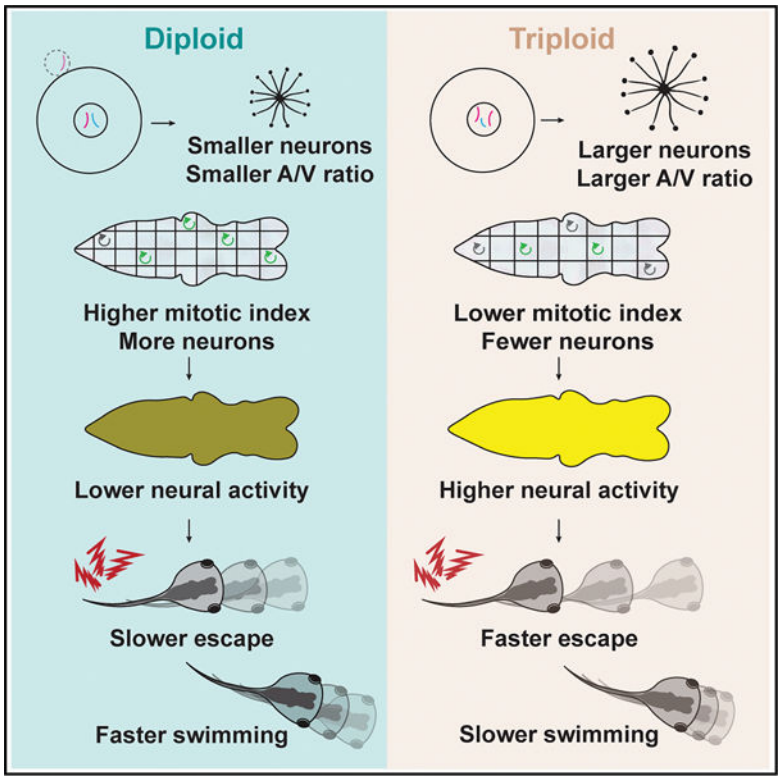
DECLARATION OF INTERESTS

The authors declare no competing interests.

DECLARATION OF GENERATIVE AI AND AI-ASSISTED TECHNOLOGIES IN THE WRITING PROCESS

During the preparation of this work, the authors used ChatGPT and DeepSeek to check for grammar, spelling, and punctuation errors. After using these tools, the authors reviewed and edited the content as needed and take full responsibility for the content of the publication.

Author Manuscript Author Manuscript Author Manuscript Author Manuscript



INTRODUCTION

Cells vary dramatically in size, yet the size of a particular cell type is relatively constant, and mechanisms are in place to ensure that cell size is properly tuned.[1,2] Previous studies indicate that cell size impacts many aspects of cell biology, including rates of biosynthesis, metabolic activity, and response to stimuli.[2] Nevertheless, the physiological consequences of cell size remain poorly understood, particularly in the brain.

Of the two main building blocks of the nervous system, neurons and glia, neurons display much larger variations in cell size over evolution.[3–5] Although underlying mechanisms are not entirely clear, one cell-size scaling factor is genome size. In amphibians, where interspecies hybridization and spontaneous polyploidization have resulted in dramatic genome size variation, a positive correlation between neuron cell body size and genome size has been demonstrated.[6–8] In *Drosophila*, fish, and mammals, somatic polyploid neurons are also associated with a larger cell body.[9–11] However, previous studies have not elucidated the effects of genome size on neuron size beyond cell body size. While the neuronal cell body (soma) supports cellular housekeeping functions and affects overall membrane potential kinetics, the neurite compartment (axon and dendrites), which contributes significantly to total cell volume, critically impacts signal propagation and connectivity. Therefore, size and shape parameters of both the cell body and the neurite compartments, including cell body size, neurite length and diameter, and neurite network complexity (Figure 1A), should be examined collectively to understand the impact of neuron size on nervous system function.

Author Manuscript Author Manuscript Author Manuscript Author Manuscript

Variation in any neuron size parameter could alter brain activity. Increased neurite diameter correlates with faster action potential kinetics,[13] while increased neurite length could mean a more extensive or expansive neurite network, leading to greater information capacity and connectivity potential.[13,14] Additionally, larger neurons with increased membrane surface area have altered capacitance and resistance and potentially harbor more ion channels and synaptic connections, resulting in reduced noise and higher temporal precision in electrical activity.[13,15–18] These properties may confer certain advantages to larger neurons. Indeed, the expansion in brain size across mammalian evolution is accompanied by a significant increase in average neuron mass.[19] In humans, larger pyramidal neurons are associated with more efficient information relay and higher IQ scores.[15] Conversely, a downward shift in neuron size is observed in the brains of patients with neurodegenerative diseases, including Alzheimer's disease,[20] Huntington's disease, and schizophrenia.[21] However, evolution does not simply select for larger neurons. In amphibians, brain complexity correlates inversely with neuron cell body size.[7,8] In birds, relative brain size decreases as genome size and cell size increase.[22,23] Additionally, increased neuron size is implicated in neurological disorders such as Lhermitte-Duclos disease and tuberous sclerosis.[24–26] Thus, our understanding of the effects of neuron size on the brain is primarily anecdotal, and more systematic approaches are needed.

In this study, we leverage *Xenopus*, a powerful model to study development and function of the vertebrate nervous system[27] as well as biological size control mechanisms,[6,28,29] to examine the links between genome size, neuron size, and neurodevelopment. By comparing individual neurons in diploid and triploid *Xenopus* embryos, we reveal how different parameters of neuron size scale with genome size. Combining imaging and flow cytometry approaches, we construct a framework to characterize how neuron size changes impact the development and function of the *Xenopus* brain. We show that triploid brains are wired with fewer, larger neurons and display a global change in neural activity, ultimately linking physiological changes at the neuron and brain levels to distinct functional behaviors at the organism level.

RESULTS

Triploid neurons are larger than diploid neurons

To generate *X. laevis* triploid embryos, we adapted established procedures[30] and cold-shocked half of each clutch of eggs shortly after fertilization to block extrusion of the second polar body, resulting in the inclusion of two sets of maternal chromosomes in addition to one set of paternal chromosomes (Figure S1A). Of note, *X. laevis* is an allotetraploid ($4n = 36$), resulting from an ancient hybridization and genome duplication event, but has evolved into a functional diploid.[31] We refer to the natural ploidy as diploid ($2n = 36$) and the cold-shocked, 1.5-fold ploidy as triploid ($3n = 54$). Consistent with previous studies,[28] triploid embryos developed at a similar rate compared with their diploid siblings, did not display physical abnormalities, and developed into normal-looking adult frogs (Figures S1A–S1C). Flow cytometry analysis of dissected, dissociated brains stained with Hoechst DNA dye confirmed the ploidy increase in triploid brains. Triploid DNA content showed a marked rightward shift to around 1.5-fold that of diploids (Figure S1D). Consistent with this,

Author Manuscript Author Manuscript Author Manuscript Author Manuscript

in toto imaging revealed a 1.5-fold increase in nuclear volume in triploid neurons compared with diploids (Figure S1E).

Across numerous cell types in all three domains of life, cell size scales positively with genome size.[32,33] Likewise, epithelial cells of experimentally induced triploid *Xenopus* tadpoles were observed to be approximately 50% larger than those of diploids.[28] However, given their highly complex morphology, neuron size is much more difficult to assess. To determine how different parameters of neuron size (Figure 1A) scale to a change in genome size, we performed sparse neuron labeling to profile the size of single neurons *in vivo*. We microinjected fluorescent-protein-encoding plasmids into brain ventricles of developing *X. laevis* embryos and used targeted electroporation to facilitate uptake by periventricular neuron progenitors,[34] which gave rise to labeled neurons that migrated into the developing brain layers.[35] Brains with single-labeled neurons were then cleared and imaged *in toto* with refractive index matching, and the imaged neurons were reconstructed in 3D (Figure 1B).

Pooling neurons by brain region, we found that total neuron volume (including cell body and neurites) was significantly greater in triploids compared with diploids (Figure 1C). We were best able to obtain images for whole, individually labeled neurons in the forebrain, where Sholl analysis comparing neurite complexity revealed the highest consistency between diploid and triploid neurons (Figure S2A), indicating that the labeled neurons belonged to similar neuronal subtypes by morphological measures. We therefore used forebrain neurons for detailed size profiling.

The increase in total volume of triploid neurons resulted from changes in the cell body and neurite compartments, with both increasing in volume approximately 1.5-fold, scaling with the 1.5-fold ploidy change (Figure 1D). Triploid neurites were significantly longer, with the total neurite length per neuron nearly double that of diploids (Figure 1E). The increased length was distributed to expand the radius of the neuron (Figure 1F) rather than to fill in the radius with more extensive arbors. Neither the number of terminal points (Figure 1G) nor the branch levels (Figure 1H) changed significantly in triploid neurons, with neurite length similarly distributed over branch levels in both ploidies (Figure S2B). These results indicate that triploid neurons do not possess distinct branching complexity or patterns compared with diploids, despite increased neurite length and volume.

Unlike other size parameters measured, triploid neurite diameter showed a subtle downward shift (Figures 1I and S2C). Thus, triploid neurons scaled up their volume by having a larger cell body and by growing neurites that were longer, but not thicker. Additionally, while other neuron size parameters showed some extent of positive correlation with total neuron volume regardless of ploidy (Figures S2D–S2G), variance in neurite diameters were explained less by cell volume and more by ploidy (Figure S2H). This suggests that decreased neurite diameter is specific to triploid neurons and may contribute to altered neuronal physiology in triploid brains.

Neuronal surface area superscales with ploidy and volume

When averaged, the decrease in neurite diameter in triploid neurons was not statistically significant (Figure 1I). However, closer examination of how neurite length was distributed

Author Manuscript Author Manuscript Author Manuscript Author Manuscript

over different diameters revealed that a larger proportion of triploid neurite length possessed smaller diameters (Figure 2A). This resulted in an increase in total neuronal cell surface area in triploids compared with diploids. Compared with the neuronal cell body, which can be roughly modeled as a sphere in which surface area subscales with volume, neurites resemble thin tubes, for which surface area superscales with volume if the diameter decreases as the volume increases (Figures 2B and 2C). Consistent with the simple geometric predictions, we observed that, while the volume of cell body and neurite compartments scaled with the 1.5-fold ploidy change (Figure 1D), the surface area of the cell body subscaled (Figure 2D, left), and the surface area of the neurites superscaled (Figure 2D, middle). Therefore, although cell volume was divided between the cell body and the neurite compartments in a similar ratio in both ploidy neurons (Figure 2E, left), cell surface area was not. A higher percentage of cell surface area was contributed by neurites in triploid neurons (Figure 2E, middle), where the differential scaling of surface-area-to-volume ratio between neurites and cell body was significantly more dramatic (Figure 2E, right). Since neurites contributed ~5× more surface area than the cell body (Figures 2D–2F), total surface area followed the trend of neurite surface area and superscaled with ploidy and cell volume (Figure 2D, right).

Triploid *Xenopus* tadpoles possess normal brain morphology

Interestingly, despite the significant increase in ploidy and neuron size, triploid brains displayed largely unaltered morphology (Figure 3A), with a similar aspect ratio (Figure 3B) and proportions of forebrain, midbrain, and hindbrain compared with diploid brains (Figures 3C and S3A). Brain size increased in triploids but only with a small effect size considering the 1.5-fold ploidy increase (Figures 3D and S3B–S3D). This change in brain size was independent of the sex of the tadpole (Figures S3E and S3F).

While the main results in this study were obtained from *X. laevis*, similar observations on how brain morphology and size change in response to an increase in ploidy were also made in *X. tropicalis*, another *Xenopus* species with a smaller genome size. In artificially induced *X. tropicalis* triploids ($3n = 30$), brain morphology and organization were largely preserved compared with diploids ($2n = 20$) (Figures S3G and S3H), and the brain size increase, although significant, was small in effect size (Figure S3I).

With larger neurons as building blocks, why are triploid brains not much larger? With imaging-based cell counting (Figure 3E) and flow cytometry of dissociated brains (Figure 3F), we observed a striking decrease in cell number in triploid brains. This 1.5-fold decrease was significant and consistent across multiple brain regions and developmental stages, thereby offsetting the neuron size increase and resulting in only a minor increase in triploid brain size.

Triploid brain cells are less proliferative but do not exhibit differences in transcription

To investigate why triploid brains contained significantly fewer cells, we utilized flow cytometry to perform DNA content-based cell-cycle analysis on cells dissociated from Hoechst-stained tadpole brains at stage 46 (Figure S1D). We found that triploid brains contained a significantly smaller proportion of G_2/M cells compared with diploids (Figure 4A), indicating reduced proliferation. To gain additional insight into the cell-cycle stages

Author Manuscript Author Manuscript Author Manuscript Author Manuscript

of the brain cells, we combined Hoechst staining with that of two cell-cycle markers, proliferating cell nuclear antigen (PCNA), an indicator of DNA replication,[38,39] and phosphohistone 3 (pH3), which labels condensed DNA during M phase.[40,41] Triple stained brains were examined by fluorescence microscopy (Figure 4B) and subsequently dissociated to obtain brain cells for flow cytometry. By microscopy, we observed distinct PCNA expression patterns in tadpole brains, which we classified as PCNA negative (G_0), PCNA diffuse, and PCNA punctate (S), respectively (Figure 4C). pH3 staining was positive only in mitotic cells that contained condensed chromosomes (Figure 4D).

Flow cytometry reliably detected these staining patterns, and combining PCNA and pH3 staining with Hoechst-based DNA content analysis enabled refinement of cell-cycle analysis to classify brain cells into individual cell-cycle phases (Figures 4E–4H and S4A–S4E). Compared with diploids, triploid brains contained a significantly larger cell population in G_1 and S phases but a significantly smaller population in G2 and M phases (Figure 4I). Triploid brains, which had not only a lower mitotic index (Figure 4I) but also a smaller total cell count (Figure 3F), contained less than half the number of mitotic cells compared with diploid brains (Figure 4J). In contrast, by caspase staining, triploid brains did not show a significant difference in cell death ratio compared with diploid brains (Figure S4F). The decreased proliferation and unaltered cell death in triploid brains indicated that they produced a smaller pool of post-mitotic neurons and glia to make up the brain. Indeed, both the percentage and the absolute number of accumulated G_0 cells were significantly lower in triploid brains (Figures 4I and 4J). Together, these data account for the decreased cell number in triploid brains and reveal a significant effect of increased ploidy and cell size on cell proliferation and cell-cycle progression.

Despite the altered cell-cycle dynamics, triploid brains showed a remarkably similar transcriptional distribution compared with diploid brains (Figures S5), indicating that triploidy, at least within one generation, does not lead to a significant imbalance in gene expression and that physiological changes observed in triploid brains were at least in part due to post-transcriptional changes caused by increased cell size.

Triploid brains display a global increase in neural activity

The fact that triploid brains are built with significantly fewer neurons compared with diploid brains indicated wiring and activity differences. With an increased surface-area-to-volume ratio, triploid neurons could possess an altered number and distribution of ion channels, changing their membrane potential control. Additionally, the increased neurite length might lead to altered connectivity.

To determine whether neural activity is impacted in triploids, we imaged brains of freely swimming stage 46 tadpoles and assessed global brain activity by the level of phospho-extracellular signal regulated kinase (pERK) in relation to the level of total ERK (Figure S6A). Phosphorylation of ERK occurs downstream of calcium signaling and is an established reporter of neural activity.[43,44] Altered pERK landscape has been reported in animal models of neurological disorders such as schizophrenia.[44,45] In tadpole brains, most pERK-expressing cells were positive for neuronal markers and had round nuclei typical of neurons rather than elongated nuclei characteristic of proliferating neuron progenitors

Author Manuscript Author Manuscript Author Manuscript Author Manuscript

(Figures S6B–S6D). Stimulation of tadpoles by tapping their dishes for 15 min was sufficient to trigger a significant alteration in pERK/ERK intensity (Figures S6E and S6F). These observations indicate that pERK/ERK staining reflects neural activity rather than changes in cell growth and proliferation.

Compared with diploids, triploid brains showed a significant increase in pERK/ERK levels in all three brain regions (forebrain, midbrain, and hindbrain) (Figures 5A and 5B), whereas ERK levels were similar (Figures 5C and 5D), consistent with our RNA sequencing (RNA-seq) (Figure S7A) and RT-PCR (Figures S7B–S7D) data showing no differential RNA expression of *X. laevis* ERK homeologs (*mapk1*.L and *mapk1*.S) between diploid and triploid brains. Together, these data suggest a global elevation in neural activity in triploid brains and support our model that physiological changes in triploid brains occur at the post-transcriptional level.

Triploid tadpoles show distinct swimming behavior compared with diploids

We next asked whether physiological differences at the brain level translated to behavioral differences at the organism level by comparing swimming behavior of diploid and triploid tadpoles (Figures 6A and S8A; Table S1). Diploid and triploid siblings were placed into side-by-side arenas, and their swimming activity was recorded following acute vibration and analyzed manually. Tadpoles were binned into three categories based on how long they stayed active during the 2-min recording. “Still” was defined as stationary or showing only very brief and unsustained swimming; “half active” was defined as showing sustained swimming for half of the time; and “active” was defined as swimming continuously throughout the recorded session (Figure 6B). For both ploidies, most tadpoles did not begin to move until 4 days post-fertilization (dpf) (stage 42–46), when the percentage of half-active tadpoles peaked. Approximately 80% of the half-active tadpoles were active during the first half of the video (Figure S8B), indicating that tadpoles at this stage swam in response to stimulation rather than spontaneously. From 5 dpf (stage 46–47) onward, most tadpoles remained active throughout the entire session. These observations are consistent with previous studies showing that, although the relevant sensory and motor systems to support simple swimming episodes are present by stage 37–39, tadpoles remain mostly stationary until stage 44–45,[46–49] while sustained spontaneous swimming likely involves the central nervous system and occurs later in development.[48] Thus, swimming behaviors of tadpoles of both ploidies follow similar developmental trajectories.

As the tadpoles became increasingly active after 4 dpf, a difference between diploid and triploid behavior emerged. A significantly lower percentage of triploid tadpoles stayed active throughout the recorded session compared with their diploid siblings on 5, 6, and 7 dpf (Figure 6B, right). Conversely, a significantly higher percentage of triploid tadpoles remained still for half or all of the recorded durations (Figure 6B, left and middle).

To determine whether triploid tadpoles swam less because their swimming behavior or apparatus was less developed or defective, we utilized the open-source algorithm TRex[50] and tracked real-time swimming speeds of individual tadpoles. As expected, tadpoles swam faster as they developed (Figure 6C, compare curves). By tracking tadpole speed over the 2-min time span following stimulation, we identified two distinct swimming modes (Figure

Author Manuscript Author Manuscript Author Manuscript Author Manuscript

6C, compare within each individual curve). Tadpoles shifted from a faster speed in the first few seconds following stimulation to a slower cruising mode when no further stimulation was applied. We denoted the first second after stimulation as the “startle” time window and the last 60 s as the “cruising” time window (Figure 6C, pink and blue boxes) and calculated the average swimming speed of tadpoles in these two windows. Compared with their diploid siblings, triploid tadpoles swam significantly faster during their startle response but significantly slower when in cruising mode (Figure 6D). Corresponding to this distinct swimming pattern during the two swimming modes, vibration stimulation elicited different responses in neural activity as reported by pERK/ERK intensity in diploid and triploid tadpoles. Across all brain regions examined, stimulation increased pERK/ERK levels in diploid brains, whereas the small increase observed in triploid brains was not statistically significant (Figures 6E and S8C; Table S2). Given that triploids swam faster during the startle period, this muted response could potentially reflect lower inhibitory modulation on the escape response after central integration of sensory inputs. Taken together, these data suggest that the increase in neuron size affects the excitability and connectivity of triploid neurons, leading to alterations in motor circuit wiring and function in triploid tadpoles.

Because early studies observed that polyploid salamanders performed worse in water-maze learning tasks,[51,52] we also examined whether repeated stimulation induced distinct learning patterns between diploid and triploid tadpoles. We did not observe differences in either startle or cruising speed across seven repetitions in one experimental session with either ploidy (Figure S8D). Thus, learning deficits with increased ploidy may be more obvious with certain species or learning tasks.

Altogether, our data indicate that differences in neuron size between the two ploidies are associated with altered cell-cycle dynamics at the cellular level, changed physiology and activity at the brain/organ level, and distinct behavioral patterns at the organism level, identifying a significant impact of cell size on the development and function of the vertebrate nervous system (Figure 7).

DISCUSSION

Neuron size beyond cell body size

Previous studies on neuron size to genome size scaling measured the cell body.[7,8] Neurite size is important in determining neuronal activity and connectivity and cannot be adequately represented by cell body size.[14,53] By profiling the size and shape of individual neurons *in vivo*, this work provides new insight into how different parameters of neuron size scale with genome size in the brain of a vertebrate. We show that neuron volume scales with genome content, with neurons maintaining their general structure and neurite-to-cell body volume ratio. This isometric scaling likely reflects intrinsic needs and regulatory mechanisms that allocate and balance volume and cellular resources between compartments to ensure operation of basic housekeeping cellular functions while achieving optimal information processing. Interestingly, the increase in neurite volume in triploid neurons is driven entirely by increased length, with a slight downward shift in triploid neurite diameter. Neurite growth requires microtubule motor-based transport, and the degree of microtubule bundling has been shown to affect the diameter and extension rate of neurites.[54,55] Fast-growing axons

Author Manuscript Author Manuscript Author Manuscript Author Manuscript

are often “stretched” and correlate with smaller diameters.[54,56] It is therefore possible that the smaller diameter of triploid neurites reflects faster extension, as they grew almost twice as much in length as diploid neurites during the 3 days following labeling. Future studies could compare neurite growth rate between ploidies, possibly in culture of isolated primary neurons, and examine whether triploid neurites catch up in diameter later in development *in vivo*.

A direct consequence of decreased neurite diameter is an increase in the surface-area-to-volume ratio. We report a 1.65-fold increase in total surface area in triploid neurons compared with diploids, superscaling with the ploidy and volume increase. This is likely an underestimate, because only smaller neurons could be profiled. The larger the neuron, the higher the proportion of both the volume and the surface area that is contributed by the neurite compartment (Figure 2F). Therefore, the surface-area-to-volume ratio of a neuron would increasingly lean toward that of its neurite compartment as neuron size increases. We estimate that, for larger neurons, the increase in surface area would approach 1.71-fold, that of the neurite compartment. Superscaling of neuronal surface area has multiple physiological implications. The expansion of surface area in relation to volume alleviates constraints on the numbers of channels, pumps, signaling molecules, and synaptic machinery that can fit on a limited membrane area,[56] impacting membrane potential control[57] as well as crucial neurodevelopmental processes, including axon guidance,[58] target recognition,[59] and synapse formation.[60] On the other hand, an increase in surface area could place a heavier burden on cellular biosynthesis and energy consumption[28,61,62] in triploid brains.

Triploid brains show a slight but significant increase in size

Organ size is determined by both the size and the number of constituent cells. Observations in the 1940s suggested that the developing kidney and eye of polyploid salamanders possessed fewer, larger cells.[63] However, whether a quantitative relationship existed between cell size and number and extended to other organs was unclear. We report that the increase in neuron size in *X. laevis* triploid brains is largely offset by a decrease in mitotic index and neuron number, resulting in a small increase in overall brain size compared with diploids. Whether effects on the cell cycle are autonomous or regulated as part of an active mechanism sensing and modulating brain size remains a fascinating question. Interestingly, brain size scales between *X. laevis* and *X. tropicalis* (compare Figures 3D and S3I), corresponding to differences in genome and cell size.[28] The disparity in how brain size responds to changes in cell size in acute versus evolutionary ploidy changes could reflect different mechanisms of organ size control. Early amphibian limb graft experiments revealed that intrinsically encoded, constitutional growth potential and extrinsic growth-regulating mechanisms (e.g., secreted proteins and adhesion molecules) co-exist in vertebrate organ size control.[64,65] It would be interesting to perform neural tube grafts between ploidies and species and observe how brain size homeostasis operates with altered extrinsic signals.

It is worth noting that the increase in brain size following the ploidy and neuron size increase is significant and non-negligible in both *X. laevis* and *X. tropicalis*. This could be a coincidence if the lowered proliferation and neuron count in triploid brains were regulated in an entirely autonomous manner. On the other hand, the fact that triploid brains do not

Author Manuscript Author Manuscript Author Manuscript Author Manuscript

grow to the exact same size as diploid brains could reflect possible physical and/or wiring constraints. For example, the increased total surface area in triploid brains could result in a larger volume of extracellular space (ECS), increasing total brain volume on top of the volume occupied by brain cells. Previous studies using *in vivo* diffusion analyses in rats and theoretical modeling have reported that ECS averages 20–60 nm in width and makes up about 20% of total brain volume.[66–68] As ECS volume scales positively with the total surface area of brain cells, it is likely that triploid brains contain a larger ECS compared with diploid brains. Moreover, the nervous system relies on intricate wiring for both development and function, and in some cases the number of essential neurons cannot simply be scaled down. An extreme example is the Mauthner cells, a pair of giant neurons located in each side of the hindbrain involved in escape behaviors.[69,70] Both diploid and triploid tadpoles have one pair of Mauthner cells (data not shown), and the connections of these neurons at the brain and spinal cord levels do not allow triploid brains to possess fewer than two. Our cell counting methods, which assess the whole brain or one brain region in bulk and provide reliable average values, would not reveal subtle and smaller-scale deviations from a reverse scaling relationship.

Ploidy and neuron size changes impact nervous system function

The drastic decrease in neuron numbers in triploid brains predicts changes in the wiring pattern and neural activity. We report a global increase in neural activity in triploid brains as read out by pERK/ERK levels. This is consistent with our model that a greater membrane surface-area-to-volume ratio changes the number and distribution of ion channels, altering membrane potential control and downstream cellular responses like ERK phosphorylation. At the organism level, we show that triploid tadpoles are more dormant and swim at a slower speed than their diploid siblings when unstimulated. Interestingly, a previous study has reported that polyploid *Ambystoma* salamanders walk a shorter distance on treadmill trials than diploids, making them inferior dispersers in nature.[71] Although neuron size and neural activity were not explored in that study, similarity with our results is unlikely to be a coincidence given the general positive scaling relationship between neuron size and genome size in amphibian species.[7]

The slower swimming speed of triploid tadpoles is likely not due to muscle deficits, since the animals were capable of sustained swimming for more than a few seconds at higher speeds and, when stimulated by vibration, could swim significantly faster than diploids. Additionally, we did not observe any morphological differences that would indicate muscle abnormalities in triploid tadpoles (Figure S1A). However, more detailed studies examining the morphology and contraction properties of muscle cells are required to determine the extent and functional impact of muscle differences.

We further show that diploid and triploid tadpoles respond differently to stimulation, both in brain activity and in swimming behavior. The response to hydrodynamic disturbance involves the mechanosensory lateral line system as well as motor nuclei within the hindbrain.[47] How the difference in vibration response between ploidies arises remains an intriguing question. For future studies, calcium imaging[72] could be utilized to assess neuronal activation before and after stimulation. Additionally, it would be interesting to test

Author Manuscript Author Manuscript Author Manuscript Author Manuscript

tadpole responses to various stimuli involving different sensory systems located in different brain regions.

Our findings highlight the functional consequences of genome and neuron size changes at both the organ and the whole-animal levels. The interplay between genome size, cell size, and cellular physiology is complex. We found little alteration in gene expression patterns between diploid and triploid brains that could account for the physiological differences observed. The similar transcriptional landscape between ploidies is not unexpected. Previous studies in yeast and mammalian cells have shown that transcription is buffered against DNA dosage and that mechanisms are in place to measure the ratio of cellular volume to DNA content.[33,73,74] In the *C. elegans* intestine, transcription is sensitive to cellular-volume-to-DNA ratio rather than to ploidy.[75] In zebrafish, comparisons among haploid, diploid, and tetraploid embryos revealed no significant transcriptional alterations across ploidies.[76] Moreover, studies in plants show that autopolyploids generally display lower alteration of gene expression due to the uniform increase in genome content and that transcription might respond to genome content change over many generations following the initial polyploidization event.[77–79] Therefore, instead of the ploidy change giving rise to transcriptional disparities, we propose that the altered neural development and function in triploid embryos stems from post-transcriptional regulation in response to changes in neuron size and shape. Taken together, the results of our work provide a framework and a tractable model for future research to further elucidate the cellular and molecular links between neuron size and neurodevelopment.

Limitations of the study

To visualize and segment individual neurons *in toto*, we utilized electroporation for sparse labeling in tadpole brains. Electroporation-mediated labeling is somewhat random, and we have limited control over which cells we label. Nevertheless, the electroporated plasmid is taken in by periventricular glia that give birth to neurons expressing the encoded fluorescent proteins. By controlling the time and position of the electric shock and the time allowed for differentiation, we can narrow the target range of neuron groups. Moreover, we used HuC/D staining to confirm the neuronal identity of labeled cells, and we pooled neurons by region and morphological similarity for comparison.

Also in this method, both the imaging speed and the maximum sample volume we could cover were limited by the desired quality and resolution, the working distance of the lens, and the fluorophore bleaching. This had two consequences. First, experimental throughput was limited. Practically, we were able to analyze only 26 diploid and 17 triploid neurons in the forebrain and even fewer in other brain regions. With this small sample size, subtle differences between diploid and triploid neurons might have been missed. Second, we could profile only smaller neurons whose neurites did not travel too far away from the cell body. However, this limitation was leveraged to our advantage, as it further narrowed down the types of neurons we profiled, making them more comparable between ploidies.

Moreover, we used phosphorylation of ERK, a downstream event of calcium influx, as a reporter to examine neural activity.[43] Traditionally, especially in mammals, expression of immediate-early genes (IEGs) like c-Fos is used to report neural activity.[80] However,

Author Manuscript Author Manuscript Author Manuscript Author Manuscript

c-Fos was not suitable for our study because of its low sensitivity,[81] variability among brain regions,[80,82] low baseline staining in fish[44] and amphibians,[83] and, practically, lack of robust antibody staining compatible with optical clearing. Upstream of IEGs,[84] pERK is a reliable marker for active neurons.[44,45,85–89] Its higher expression allows assessment of baseline neural activity in unstimulated brains, and co-staining with total ERK provides a control to normalize staining variability. However, while an established reporter, pERK staining requires fixation and is limited in its temporal resolution. Additionally, while our data show that pERK levels respond to extrinsic stimuli triggering neural activity, pERK staining cannot reveal detailed electrical properties of diploid and triploid neurons. Future electrophysiological[90] studies are required to determine how triploid neurons achieve altered homeostasis, since decreased neurite diameter is expected to impede signal propagation, while increased soma size and neurite length could enhance connectivity and potentially shift the excitatory/inhibitory balance.

RESOURCE AVAILABILITY

Lead contact

Requests for further information and resources should be directed to and will be fulfilled by the lead contact, Xiao Liu (xiao.liu@berkeley.edu).

Materials availability

This study did not generate new unique reagents. All materials used are available upon request.

Data and code availability

- All data reported in this paper will be shared by the lead contact upon request.
- This paper does not report original code.
- Any additional information required to reanalyze the data reported in this paper is available from the lead contact upon request.

STAR★METHODS

EXPERIMENTAL MODEL AND STUDY PARTICIPANT DETAILS

Xenopus *frogs and embryos*: All *Xenopus* frogs and embryos were used and maintained following standard protocols established by the UC Berkeley Animal Care and Use Committee and approved in our Animal Use Protocol (approval number: AUP-2014–08-6596–3).

Mature *X. laevis* and *X. tropicalis* were obtained from Nasco (Fort Atkinson, WI) or the National *Xenopus* Resource Center (Woods Hole, MA), and were housed in a recirculating tank system with regularly monitored temperature and water quality, with *X. laevis* at 20–23°C and *X. tropicalis* at 23–26°C. All animals were fed Nasco frog brittle.

X.laevis and *X. tropicalis* females were ovulated with no harm to the animals with a minimum 4-months rest interval. To obtain testes for *in vitro* fertilizations, *X. laevis*

Author Manuscript Author Manuscript Author Manuscript Author Manuscript

and *X. tropicalis* males were euthanized by over-anesthesia through immersion in 0.05% benzocaine in double-distilled water (ddH_2O) prior to dissection. Carcasses were frozen at −20°C. Tadpoles were euthanized in 0.01‰ benzocaine in ddH_2O prior to fixation.

Experiments in this study used both male and female embryos/tadpoles in a mixed population. Potential influence of sex is discussed in the Results section.

METHOD DETAILS

***In vitro fertilization of* X. laevis *and* X. tropicalis:** *Xenopus in vitro* fertilizations were performed as previously described[30]. Briefly:

I. To prepare for fertilization, *X. laevis* females were primed with 100 U of pregnant mare serum gonadotropin (PMSG) (Calbiochem #367222). 2–14 days after priming, in the afternoon before the experiment, primed females were boosted with 500 U of human Chorionic Gonadotropin (hCG) (either Sigma #CG10, or Chorulon Merck #133754) and kept at 16°C overnight in 1X MMR (100 mM NaCl, 2 mM KCl, 2 mM $CaCl_2$, 1 mM $MgSO_4$, 0.1 mM EDTA, 5 mM HEPES-NaOH, pH 7.6). *X. tropicalis* females were primed with 10 U hCG 14–16 h before boosting, kept at room temperature in ddH_2O, and boosted with 250 U the morning of the experiment. Testes were dissected from euthanized males and, for *X. laevis*, kept at 4°C in 1X MR (100 mM NaCl, 1.8 mM KCl, 1 mM $MgCl_2$, 5 mM HEPES-NaOH, pH 7.6) or, for *X. tropicalis*, placed in 1X MBS (88 mM NaCl, 1.006 mM KCl, 2.49 mM $NaHCO_3$, 0.998 mM $MgSO_4$, 5 mM HEPES-NaOH, pH 7.8) with 0.2% Bovine Serum Albumin (BSA) and used the same day.

II. To perform fertilization, eggs were collected by gently squeezing females atop a 60 mm petri dish. Sperm solution was prepared by homogenizing a small piece of testis in a 1.7 mL Eppendorf tube using a plastic pestle (~1/4 of a testis in 1 mL of 1/10X MMR for *X. laevis*, or ~1/2 of a testis in 0.5 mL of 0.2% BSA in 1X MBS for *X. tropicalis).* The sperm solution was added to the egg dish and the eggs were gently swirled until they formed a monolayer at the bottom of the dish, incubated for 10 min (*X. laevis*) or 4 min *(X. tropicalis)* with the dish slightly tilted to ensure submersion of eggs, and then flooded with 1/10X MMR (*X. laevis*) or ddH_2O *(X. tropicalis).*

III. To obtain triploids, embryos were cold shocked at 13 min (*X. laevis*) or 9 min *(X. tropicalis)* post fertilization by exchanging the room temperature buffer with pre-chilled 4°C 1/10X MMR and putting the dish in a slushy ice bath for 15 min. After the cold shock, embryos were equilibrated in room temperature 1/10X MMR for at least 5 min. For each triploid dish, a control diploid dish was made by proceeding directly from the fertilization steps (II) to the de-jellying steps (IV).

IV. To remove jelly coats, embryos were incubated in freshly prepared De-jellying Solution (3% L-cysteine in ddH2O-NaOH, pH 7.8) for about 10 min, and then washed 5X with 1/10X MMR.

Author Manuscript Author Manuscript Author Manuscript Author Manuscript

Maintenance and staging of *Xenopus* embryos: Fertilized and de-jellied embryos were transferred to larger dishes (100 mm diameter X 15 mm high) and kept in 1/10X MMR in incubators set at 23°C (for *X. laevis*) or 24°C (for *X. tropicalis*). Dead or lysed embryos were removed, and media was exchanged with fresh 1/10X MMR twice a day for the first two days and at least once a day afterwards. Diploid and triploid embryos were maintained at the same density and media levels.

Tadpoles were euthanized and staged before experiments according to the Nieuwkoop and Faber development table[107].

Tadpole sex determination: PCR-based sex determination was performed as previously described[28,91]. Tails of individual euthanized tadpoles were cut, transferred to 20 μL of 1X Phusion buffer (New England Biolabs #E0553S) in 200 μL PCR tubes, frozen at −80°C for >1 h, thawed, spun down, and boiled at 95°C for 10 min. Next, 2.5 μL of 20 ng/mL Proteinase K (New England Biolabs #P8107S) was added to each tube and the tubes were incubated at 55°C for 4 h, boiled at 95°C for 10 min, and stored at 4°C. 2.5 μL of the lysis solution was used as template in the subsequent PCR reaction, which was performed using the Phusion High-Fidelity PCR kit (New England Biolabs E0553S), forward (AAAACCATGACCTCCCGGATAC) and reverse (TAGGGAGGGGTTTGGAGGTTC) primers[91], with 35 cycles annealing at 58°C for 30 s and elongating at 72°C for 30 s.

Tadpole brain immunofluorescence and clearing: Immunofluorescence and clearing was performed combining protocols from Helen Willsey's lab (UCSF, CA) and Affaticati et al[108]. Euthanized tadpoles were fixed in 4% PFA in PBS at 4°C overnight and washed 4X with PBS. For *X. laevis*, 5–10 brains of staged tadpoles were dissected using two pairs of fine-tip tweezers and collected in 500 μL of PBS in a 1.7 mL Eppendorf tube. For *X. tropicalis*, 5–7 tadpoles were directly collected without brain dissection.

To bleach the samples, 500 μL of 2X Bleaching Solution (1X: 10% formamide, 8% hydrogen peroxide in PBS) was added to each tube and the tubes were placed in a light-colored rack under bright light for 1.5 h. Bleached samples were washed extensively (>4X) with PBST, incubated in fresh PBST overnight at 4°C, blocked and permeabilized with 50 μL of Blocking Buffer (10% goat serum (Jackson ImmunoResearch #005–000-001), 10% DMSO, and 1% Triton X-100 in PBST) for 2–4 h at room temperature, and then incubated with primary antibodies in 50 μL of Staining Buffer (2% goat serum, 10% DMSO, 0.1% Triton X-100, and 0.05% sodium azide in PBST) for 2–3 days at 4°C. Next, samples were washed three times each for >20 min with PBST at room temperature and incubated with secondary antibodies along with 10 ng/mL Hoechst 33342 (Thermo Fisher Scientific #H3570) in 50 μL of Staining Buffer for 1–2 days at 4°C, with the tubes wrapped in foil to avoid light. All incubations were carried out on a nutator. All primary and secondary antibodies were used at 1:250 including mouse anti-HuC/HuD (Thermo Fisher Scientific #A-21271), mouse anti-β-tubulin (DSHB E7 concentrate form), mouse anti-PCNA (Thermo Fisher Scientific #13–3900), mouse anti-p44/42 MAPK Erk1/2 (Cell Signaling #4696), rabbit anti-phospho-p44/42 MAPK Erk1/2 (Thr202/Tyr204) (Cell Signaling #4370), rabbit anti-phospho-Histone H3 (Ser10) (Millipore Sigma #06–570), rabbit anti-RFP (Abcam

Author Manuscript Author Manuscript Author Manuscript Author Manuscript

#ab62341), rabbit anti-cleaved caspase-3 (Cell Signaling #9661), Alexa Fluor 488 goat anti-mouse IgG (Thermo Fisher Scientific #A-11001), Alexa Fluor 568 goat anti-mouse IgG (Thermo Fisher Scientific #A-11004), Alexa Fluor 488 goat anti-rabbit IgG (Thermo Fisher Scientific #A-11008), and Alexa Fluor 568 goat anti-rabbit IgG (Thermo Fisher Scientific #A-11011).

To clear samples after the immunostaining steps, fructose-based high-refractive index solution (fbHRI) was prepared by mixing 4 parts of F1457 (90% fructose in fbHRI diluent (0.2X PBS, 0.002% sodium azide), refractive index (RI) 1.457) with 1 part of DMSO1457 (85% DMSO in fbHRI diluent, RI 1.457) and adjusting RI to 1.457 with 100% fructose/fbHRI diluent. Stained samples were washed three times each for >20 min with PBST at room temperature on a nutator, incubated for >2 h in PBST, exchanged into 50% fbHRI in fbHRI diluent, incubated for >6 h at 4°C, exchanged into fbHRI, and incubated for >12 h at 4°C. Cleared samples were stored in fbHRI, avoiding light, at 4°C until imaging, for up to a few weeks.

In toto imaging of whole-mount brains: Stained and cleared brains (for *X. laevis*) or tadpoles (for *X. tropicalis)* were mounted in fbHRI onto small glass bottom dishes (MatTek # P35G-1.5–14-C), with the dorsal side facing down. Extra liquid was removed so that the brain would lay flat on the glass bottom. Confocal imaging was performed on an inverted ZEISS LSM 800 using the ZEISS ZEN 2.3 (Blue edition) software, with a Plan-Apochromat 10X/0.45 air objective (for brain size and morphology measurements), a Plan-Apochromat 20X/0.8 air objective (for pERK/ERK intensity measurements), or a Plan-Apochromat 40x/1.2 Imm Corr DIC glycerine immersion objective (for nucleus counting, nuclear volume measurements, and single neuron imaging), with a pinhole size set at 1 Airy Unit. In experiments quantifying and comparing fluorescence intensity, all laser settings were kept the same for diploid and triploid samples and images were taken in 16-bit. Post-hoc brightness/contrast adjustments, if any, were always applied uniformly across diploid and triploid samples. In experiments where fluorescence intensity was not quantified, laser settings were adjusted separately utilizing the Range Indicator Tool in the ZEN software for optimal visualization, and brightness/contract adjustments may differ between samples for presentation purposes. Image stitching, when needed, was performed either with the built-in Tile Function of the ZEN software, or the Stitching Plugin[101] of the FIJI software[99].

Sparse labeling and single neuron reconstruction: Electroporation was performed mostly following protocols from Hollis Cline's lab[34,35]. On 4 dpf, stage 44 tadpoles were anesthetized in 0.01‰ benzocaine in 1/10X MMR for several minutes and transferred to a wet tissue on top of an inverted petri dish. 20–30 nL of Injection Mix (350–400 ng/μL pCMV-RFP plasmid, 0.2% Brilliant Blue dye in EB buffer) was injected into the brain ventricle of each tadpole using needles pulled from glass capillaries (World Precision Instruments #TW100F-4), mounted on a Narishige micromanipulator, and connected to a Picospritzer III Microinjection Dispense System. Next, a pair of platinum electrodes, cut from Sutter puller filaments, controlled by another Narishige micromanipulator, and connected to a Grass SD9 Stimulator, were positioned to clamp the desired brain region

Author Manuscript Author Manuscript Author Manuscript Author Manuscript

of the injected tadpole. Two 30V, 1.6 ms pulses each polarity were delivered through the electrodes.

Electroporated tadpoles were transferred to large dishes with fresh 1/10X MMR in a well-ventilated area for recovery. When movement was observed again, tadpoles were put back into 23°C incubators and allowed to rest for 3 days. On 7 dpf, tadpoles were euthanized and fixed, and their brains dissected, stained with anti-RFP and anti-HuC/D antibodies, cleared, and imaged as described earlier. Diploid and triploid samples to be compared were always processed in parallel through the injection, electroporation, recovery and subsequent staining and imaging steps.

Labelled single cells with confirmed neuronal identity (HuC/D positive) were reconstructed with Imaris 10.2.0 (license owned by CRL Molecular Imaging Center, UC Berkeley) semi-automatically based on the immunostaining-amplified RFP signal, with the Surfaces Function to remove background signal and the Filaments Function to reconstruct the soma model and neurite paths (with soma as starting point and no loops). Parameters and settings in automatic programs were kept constant between all processed neurons when possible, and manual supervision and model training were performed with best judgement. After reconstruction, all measurements were exported and analyzed with R 4.2.1[92].

Imaging-based brain measurements: For nucleus counting and nuclear volume measurements, brains were dissected, stained with anti-PCNA and anti-caspase-3 antibodies and Hoechst, and cleared as described earlier. Whole-mount brains were imaged with confocal microscopy as described earlier except that the Auto Z Brightness Correction Function in the ZEN software was used to compensate for dimmer fluorescence in deeper tissues. Two 159.73 μm X 159.73 μm X 100 μm regions of interest (ROIs) in left and right forebrain and a 319.45 μm X 319.45 μm X 50 μm ROI in hindbrain were cropped from the image stack of each brain. Similar regions were cropped across all processed brains using morphological landmarks as reference. ROI was not taken in midbrain because light refraction across the midbrain ventricle caused images to be less sharp. Single nuclei were segmented with Cellpose[106] using the Cyto Model based on the Hoechst channel. Segmented nuclei were counted and measured using the 3DSuite Plugin[100] of the FIJI software[99]. A home-built code in R 4.2.1[92] was used to remove measurements of nuclei positive for PCNA (progenitors, not neurons) or at ROI borders. Caspase positive nuclei were counted manually because the labelling was sparse.

For brain morphology measurements, dissected brains (for *X. laevis*) or tadpoles (for *X. tropicalis)* were stained with anti-β-tubulin antibody and Hoechst and imaged as described earlier except that to avoid potential shrinkage, samples were not cleared and were mounted and imaged in PBST. Forebrain, midbrain, and hindbrain ROIs were traced manually using the Freehand Selections Tool in FIJI[99]. Sample identity was masked during this process to minimize bias. All measurements were exported and analyzed with R 4.2.1[92].

Flow cytometry and cell cycle analysis: Dissected brains from tadpoles of the correct stage were processed for staining (with Hoechst, with or without anti-PCNA and anti-PH3 antibodies) as described above without the clearing steps. To dissociate the stained brains, 5–

Author Manuscript Author Manuscript Author Manuscript Author Manuscript

6 brains were transferred to 100 μL of Dissociation Buffer (90% StemPro Accutase (Thermo Fisher Scientific #A1110501), 0.05% Triton X-100, in PBS) in a 1.7 mL low retention Eppendorf tube and incubated at room temperature, avoiding light, overnight. The Accutase reaction was stopped by adding 250 μL of PBS to the tube and the brains were further physically dissociated by pipetting up and down for 30 s. 20 μL of CountBright Absolute Counting Beads (Thermo Fisher Scientific #C36950, LOT #2361081, $0.52*10^5$ beads/50 μL) were added to each tube, mixed with the solution by pipetting up and down 10 times, and the whole mixture was transferred to a 12 mm X 75 mm CellPro flow cytometry tube through a 35 μm mesh strainer cap (Alkali Scientific #CT6405). The Eppendorf tube was washed twice each with 250 μL of 1X HBSS, and the washing liquid was also transferred through the mesh to the flow cytometry tube. Flow cytometry tubes were kept on ice, avoiding light, until the flow cytometry run. Low retention pipet tips were used throughout.

Each tube of dissociated brain cells was vortex briefly and run with a BD LSR Fortessa X-20 Cell Analyzer (CRL Flow Cytometry Facility, UC Berkeley). Pacific Blue channel was used for detecting Hoechst staining, and FITC channel for Alexa Fluor 488, PE-Texas Red channel for Alexa Fluor 568, APC-cy7 channel for the rainbow-colored counting beads. A tube of dissociated brain cells with beads added but without any staining was included in each run to facilitate gate drawing. FlowJo 10.8.1 (Becton Dickinson & Company) was used for processing the flow cytometry data. All events were gated with forward scatter width over forward scatter area (FSC-W/FSC-A) for singlets. Singlets were separated into a “Beads” and a “Non-beads” population based on APC-cy7 channel intensity. The “Non-beads” population was further gated first with side scatter width over side scatter area (SSC-W/SSC-A) and then Hoechst intensity to ensure that they were single cell events. Next, for any one sample to pass the post-hoc quality control (QC) performed with a home-built code in R 4.2.1[92], the following conditions were met: a) sample had > 5,000 bead events; b) sample had >10,000 single cell events; c) sample mean of FSC-A and Pacific Blue channel intensity of bead events fell inside run mean*(1±CV) of all bead events; d) sample CV of FSC-A and Pacific Blue channel intensity of bead events was less than 2X run CV of all bead events; and e) sample had a corresponding diploid/triploid sample to compare to. These gating and QC steps were performed in an unbiased way across all diploid and triploid samples in each run.

For cell counting, number of cells per brain (N) was calculated as:

$$N = \frac{N_{Single\ cell\ event}}{N_{Bead\ event} * N_{Brain}} * \frac{0.52 * 10^5}{50} * 20$$

For initial cell cycle analysis (Figure 4A), FlowJo built-in Cell Cycle Tool was used on single cell populations with the following settings: Pacific Blue channel (Hoechst), Dean Jett Fox (DJF) model[42], no synchronized peak, no peak constraints. For further cell cycle analysis combining PCNA and pH3 staining (Figures 4E–4G and S5), a home-built R 4.2.1[92] code was used to fit Gaussian peaks under probability density curves of logarithmic PCNA and pH3 intensities. Areas of each fitted peak were calculated as fractions of the corresponding population (Figures 4E and 4F).

Author Manuscript Author Manuscript Author Manuscript Author Manuscript

pERK/ERK intensity measurements: To measure baseline neural activity, unstimulated, freely swimming tadpoles were over-anesthetized in 0.05% benzocaine for 1 min and immediately processed for fixation. Corning Netwell Strainers were used to enable efficient buffer exchanges to minimize disturbance of tadpoles and potential impact on neural activity. Brains of stage 46 tadpoles were dissected, stained with anti-ERK and anti-pERK antibodies and Hoechst, cleared, and imaged as described earlier. Tiled images of each brain were auto-stitched into a 640.15 μm X 1790.04 μm z-stack in ZEISS ZEN and then analyzed with FIJI[99]. 170 z-slices across 150 μm from the top surface of the brain were summarized to a z-projection and registered to one reference brain projection generated from a representative, normal-looking stage 46 diploid brain using the bUnwarpJ Plugin[102]. With the registered images, pERK intensity was normalized to ERK intensity using the Image Calculator Function, and the normalized result was masked to remove background signal outside the brain sample area with a mask generated by thresholding the ERK channel with the “Huang” method followed by “Process>Binary>Fill holes”. ROIs of different brain regions manually traced with the Freehand Selections Tool on the reference projection were used for intensity measurements. To adjust for clutch variance, diploid images of each clutch were averaged, and the maximum intensity of the averaged image was used to normalize all measurements of that clutch. The summary images presented (Figures 5 and S7D) were averaged from clutch averages.

To measure neural activity after stimulation, all procedures were the same as above except that prior to euthanasia, tadpoles were split evenly between a stimulation dish and a control dish, with the former either manually tapped on bench top continuously for 15 min (Figures S6D and S6E) or stimulated with a computer program-controlled dental vibrator as in the swimming assay (Figure 6E), and the latter placed on the farthest bench in the same room to avoid disturbance from the tapping/vibration noise. Maximum intensity of control averages of each clutch was used to normalize against clutch variance. Control data in the tapping experiment (3 clutches, Figures S6E and S6F) were also included as diploid data in the unstimulated dataset (6 clutches, Figure 5).

Brain-specific RNA-seq and RT-PCR: J strain (37 generations inbred) *X. laevis* obtained from National *Xenopus* Resource were used to prepare samples for RNA-seq experiments. In the afternoon on 4 dpf, tadpoles were over-anesthetized in 0.05% benzocaine in 1/10X MMR for 1 min and immediately processed for dissection. For each replicate, >10 brains per ploidy of stage 44–46 tadpoles from the same clutch were dissected using two pairs of fine-tip tweezers and immediately transferred to a 1.7 mL Eppendorf tube containing 100 μL of PBS and 400 μL of TRIzol (Invitrogen #15596026). Tubes containing dissected brains were kept on ice during dissection, fast frozen with liquid N_2 immediately after dissection, and kept at −80°C.

To extract RNA, brains were subjected to 3 cycles of freeze-thaw with liquid N_2 and a 37°C water bath and incubated at room temperature for 5 min. Next, 80 μL of chloroform was added to each tube and the mixture was inverted several times for 15 s, incubated at room temperature for 3 min, transferred to a Phasemaker tube (Invitrogen # A33248), and spun at 12,000 g at 4°C for 15 min. The aqueous phase was transferred to a new 1.7 mL Eppendorf tube, mixed with 200 μL of isopropanol, incubated at room temperature for 10 min, and

Author Manuscript Author Manuscript Author Manuscript Author Manuscript

spun at 12,000 g at 4°C for 10 min. After carefully removing the supernatant, the pallet was washed with 400 μL of pre-chilled 75% ethanol twice, air-dried for 5 min on ice, and resuspended in 44 μL of RNase-free water. Potential DNA contaminant was removed by incubating with 5 μL of 10X DNase I buffer and 1 μL of DNase I (NEB #M0303S) at 37°C for 10 min, and RNA was purified using the Monarch RNA Cleanup Kit (NEB #T2040S).

For RNA-seq, RNA quality control, library preparation (Kapa Biosystems library preparation kits with covaris/bioruptor shearing for gDNA, custom Unique Dual Indexes to eliminate cross sample bleed), and sequencing (NovaSeq 6000 S4, 150 bp paired-end reads, 25M reads per sample) was performed by QB3 Genomics, UC Berkeley. Sequencing results were fastQC-ed[103], quality trimmed with Trim Galore[104], and aligned to reference transcriptome (*Xenopus laevis* v10.1) with Salmon[105] in Linux. Data from Salmon was imported to DESeq2 using TXimport[97] and differential expression analysis was performed with DESeq2[98] in R 4.2.1[92].

For RT-PCR, reverse transcription was performed using the iScript cDNA Sythesis Kit (Bio-Rad # 1708890), and RT-PCR was performed with the iTaq Universal Probes Supermix (Bio-Rad #1725130) on a Bio-Rad CFX96 Touch Real-Time PCR Machine with the synthesized cDNA as template and the following custom-made RT-PCR assays ordered from IDT: 1) mapk1. Forward: CTCATCCTTATCTGGAGCAGTATTAT; Reverse: AGTGTCTCCTTGGGCAAATC; Probe: /56-FAM/ACCCAAGTG/ZEN/ATGAGCCTGTAGCTG/3IABkFQ/. 2) gapdh. Forward: CAGCAGAGGGACCAATGAAA; Reverse: CGGCATCAAAGATGGAGGAATA; Probe: /56-FAM/ACACACAAG/ZEN/ACCAGGTTGTCTCCA/3IABkFQ/. 3) rpl8. Forward: CAGGTCGTGCCTACCATAAAT; Reverse: CCTGATGGTTGAGGGCTTAC; Probe: /56-FAM/TGGTGTGGC/ZEN/TATGAACCCTGTTGA/3IABkFQ/.

Tadpole swimming assay: The tadpole swimming assay setup (Figure 6A) was inspired by a protocol from Lopez et al[109]. For each session, 6 tadpoles each ploidy from the same clutch were placed in 1/10X MMR in a pair of swimming arenas, made from 100 mm X 100 mm clear plastic dishes, arranged side by side, lighted from below with an LED screen, and attached to a computer-controlled dental vibrator. Each session consisted of 7 consecutive repeats, in each of which tadpoles were stimulated by a brief, strong vibration, recorded for 2 min by a GoPro camera fixed above the arenas, and allowed to rest without stimulation for another 3 min. Tadpoles were euthanized afterwards, and different groups of 6 tadpoles each ploidy were used for sessions at different time points. Tadpole swimming in the recorded videos was first scored manually based on activity level, and then traced automatically with the open-source algorithm TRex[50]. Next, measurements were exported and analyzed with R 4.2.1[92]. The detailed time scheme and number of replicates used are reported in Figure S9A.

QUANTIFICATION AND STATISTICAL ANALYSIS

Software used in each experiment is described in the Method Details section.

Statistical details—including statistical tests used, exact value of n, what n represents, definition of center, dispersion and precision measures, exclusion of any data or subjects, and how statistical significance was defined—can be found in the figure legends.

Author Manuscript Author Manuscript Author Manuscript Author Manuscript

Supplementary Material

Refer to Web version on PubMed Central for supplementary material.

ACKNOWLEDGMENTS

We thank Marla Feller, Helen Bateup, Meng-meng Fu, Marc Hammarlund, Coral Zhou, Helena Cantwell, Gabriel Cavin-Meza, Kevin Williams, and Shenliang Yu for feedback on the manuscript; Helen Willsey, Kate McCluskey, Na Ji, and Gokul Upadhyayula for discussion and suggestions on reagents and methodology; Caroline McKeown (Hollis Cline lab, Scripps) for advice on electroporation; Shaina Carroll (Barton lab, UC Berkeley) and Kartoosh Heydari (CRL Flow Cytometry Facility, UC Berkeley) for help with flow cytometry experiments; Michael Jacob Abrams (Harland lab, UC Berkeley) for allowing us to use their RT-PCR machine; Virgilio López III (Carlos Aizenman lab, Brown University) for advice on tadpole swimming assays; and Martin Ziyuan Liu and the animal facility of UC Berkeley for frog care. R.H. was supported by NIH Maximizing Investigators' Research Award grant R35GM118183652 and the Flora Lamson Hewlett Chair in Biochemistry.

REFERENCES

1. Lloyd AC (2013). The Regulation of Cell Size. Cell 154, 1194–1205. 10.1016/j.cell.2013.08.053. [PubMed: 24034244]
2. Ginzberg MB, Kafri R, and Kirschner M (2015). On being the right (cell) size. Science 348, 1245075. 10.1126/science.1245075. [PubMed: 25977557]
3. Azevedo FAC, Carvalho LRB, Grinberg LT, Farfel JM, Ferretti REL, Leite REP, Jacob Filho W, Lent R, and Herculano-Houzel S (2009). Equal numbers of neuronal and nonneuronal cells make the human brain an isometrically scaled-up primate brain. J. Comp. Neurol. 513, 532–541. 10.1002/cne.21974. [PubMed: 19226510]
4. Herculano-Houzel S (2014). The glia/neuron ratio: how it varies uniformly across brain structures and species and what that means for brain physiology and evolution. Glia 62, 1377–1391. 10.1002/glia.22683. [PubMed: 24807023]
5. Mota B, and Herculano-Houzel S (2014). All brains are made of this: a fundamental building block of brain matter with matching neuronal and glial masses. Front. Neuroanat. 8, 127. 10.3389/fnana.2014.00127. [PubMed: 25429260]
6. Levy DL, and Heald R (2015). Biological Scaling Problems and Solutions in Amphibians. Cold Spring Harb. Perspect. Biol. 8, a019166. 10.1101/cshperspect.a019166. [PubMed: 26261280]
7. Roth G, and Walkowiak W (2015). The Influence of Genome and Cell Size on Brain Morphology in Amphibians. Cold Spring Harb. Perspect. Biol. 7, a019075. 10.1101/cshperspect.a019075. [PubMed: 26261281]
8. Roth G, Blanke J, and Wake DB (1994). Cell size predicts morphological complexity in the brains of frogs and salamanders. Proc. Natl. Acad. Sci. USA 91, 4796–4800. 10.1073/pnas.91.11.4796. [PubMed: 8197137]
9. Nandakumar S, Grushko O, and Buttitta LA (2020). Polyploidy in the adult Drosophila brain. eLife 9, e54385. 10.7554/eLife.54385. [PubMed: 32840209]
10. Nandakumar S, Rozich E, and Buttitta L (2021). Cell Cycle Re-entry in the Nervous System: From Polyploidy to Neurodegeneration. Front. Cell Dev. Biol. 9, 698661. 10.3389/fcell.2021.698661. [PubMed: 34249947]
11. Sigl-Glöckner J, and Brecht M (2017). Polyploidy and the Cellular and Areal Diversity of Rat Cortical Layer 5 Pyramidal Neurons. Cell Rep. 20, 2575–2583. 10.1016/j.celrep.2017.08.069. [PubMed: 28903039]
12. Desmet A-S, Cirillo C, and Vanden Berghe P (2014). Distinct subcellular localization of the neuronal marker HuC/D reveals hypoxia-induced damage in enteric neurons. Neuro Gastroenterol. Motil. 26, 1131–1143. 10.1111/nmo.12371.
13. Yu L, and Yu Y (2017). Energy-efficient neural information processing in individual neurons and neuronal networks. J. Neurosci. Res. 95, 2253–2266. 10.1002/jnr.24131. [PubMed: 28833444]

Author Manuscript Author Manuscript Author Manuscript Author Manuscript

14. Pannese E (2015). III. Shape and Size of Neurons. In Neurocytology: Fine Structure of Neurons, Nerve Processes, and Neuroglial Cells, Pannese E, ed. (Springer International Publishing), pp. 13–23. 10.1007/978-3-319-06856-5_3.
15. Goriounova NA, Heyer DB, Wilbers R, Verhoog MB, Giugliano M, Verbist C, Obermayer J, Kerkhofs A, Smeding H, Verberne M, et al. (2018). Large and fast human pyramidal neurons associate with intelligence. eLife 7, e41714. 10.7554/eLife.41714. [PubMed: 30561325]
16. Kosillo P, Doig NM, Ahmed KM, Agopyan-Miu AHCW, Wong CD, Conyers L, Threlfell S, Magill PJ, and Bateup HS (2019). Tsc1-mTORC1 signaling controls striatal dopamine release and cognitive flexibility. Nat. Commun. 10, 5426. 10.1038/s41467-019-13396-8. [PubMed: 31780742]
17. Kosillo P, Ahmed KM, Aisenberg EE, Karalis V, Roberts BM, Cragg SJ, and Bateup HS (2022). Dopamine neuron morphology and output are differentially controlled by mTORC1 and mTORC2. eLife 11, e75398. 10.7554/eLife.75398. [PubMed: 35881440]
18. Bateup HS, Johnson CA, Denefrio CL, Saulnier JL, Kornacker K, and Sabatini BL (2013). Excitatory/inhibitory synaptic imbalance leads to hippocampal hyperexcitability in mouse models of tuberous sclerosis. Neuron 78, 510–522. 10.1016/j.neuron.2013.03.017. [PubMed: 23664616]
19. Herculano-Houzel S, Manger PR, and Kaas JH (2014). Brain scaling in mammalian evolution as a consequence of concerted and mosaic changes in numbers of neurons and average neuronal cell size. Front. Neuroanat. 8, 77. 10.3389/fnana.2014.00077. [PubMed: 25157220]
20. Rinne JO, Paljärvi L, and Rinne UK (1987). Neuronal size and density in the nucleus basalis of Meynert in Alzheimer's disease. J. Neurol. Sci. 79, 67–76. 10.1016/0022-510x(87)90260-7. [PubMed: 3612173]
21. Rajkowska G, Selemon LD, and Goldman-Rakic PS (1998). Neuronal and glial somal size in the prefrontal cortex: a postmortem morphometric study of schizophrenia and Huntington disease. Arch. Gen. Psychiatry 55, 215–224. 10.1001/archpsyc.55.3.215. [PubMed: 9510215]
22. Andrews CB, and Gregory TR (2009). Genome size is inversely correlated with relative brain size in parrots and cockatoos. Genome 52, 261–267. 10.1139/G09-003. [PubMed: 19234554]
23. Gregory TR (2018). Genome size and brain cell density in birds. Can. J. Zool. 96, 379–382. 10.1139/cjz-2016-0306.
24. Backman SA, Stambolic V, Suzuki A, Haight J, Elia A, Pretorius J, Tsao M-S, Shannon P, Bolon B, Ivy GO, and Mak TW (2001). Deletion of Pten in mouse brain causes seizures, ataxia and defects in soma size resembling Lhermitte-Duclos disease. Nat. Genet. 29, 396–403. 10.1038/ng782. [PubMed: 11726926]
25. Kwon C-H, Zhu X, Zhang J, Knoop LL, Tharp R, Smeyne RJ, Eberhart CG, Burger PC, and Baker SJ (2001). Pten regulates neuronal soma size: a mouse model of Lhermitte-Duclos disease. Nat. Genet. 29, 404–411. 10.1038/ng781. [PubMed: 11726927]
26. Bassetti D, Luhmann HJ, and Kirischuk S (2021). Effects of Mutations in TSC Genes on Neurodevelopment and Synaptic Transmission. Int. J. Mol. Sci. 22, 7273. 10.3390/ijms22147273. [PubMed: 34298906]
27. Exner CRT, and Willsey HR (2021). Xenopus leads the way: Frogs as a pioneering model to understand the human brain. Genesis 59, e23405. 10.1002/dvg.23405. [PubMed: 33369095]
28. Cadart C, Bartz J, Oaks G, Liu MZ, and Heald R (2023). Polyploidy in Xenopus lowers metabolic rate by decreasing total cell surface area. Curr. Biol. 33, 1744–1752.e7. 10.1016/j.cub.2023.03.071. [PubMed: 37080197]
29. Brownlee C, and Heald R (2019). Importin α Partitioning to the Plasma Membrane Regulates Intracellular Scaling. Cell 176, 805–815.e8. 10.1016/j.cell.2018.12.001. [PubMed: 30639102]
30. Gibeaux R, and Heald R (2019). Generation of Xenopus Haploid, Triploid, and Hybrid Embryos. Methods Mol. Biol. 1920, 303–315. 10.1007/978-1-4939-9009-2_18. [PubMed: 30737699]
31. Session AM, Uno Y, Kwon T, Chapman JA, Toyoda A, Takahashi S, Fukui A, Hikosaka A, Suzuki A, Kondo M, et al. (2016). Genome evolution in the allotetraploid frog Xenopus laevis. Nature 538, 336–343. 10.1038/nature19840. [PubMed: 27762356]
32. Mueller RL (2015). Genome Biology and the Evolution of Cell-Size Diversity. Cold Spring Harb. Perspect. Biol. 7, a019125. 10.1101/cshperspect.a019125. [PubMed: 26254312]

Author Manuscript Author Manuscript Author Manuscript Author Manuscript

33. Darmasaputra GS, van Rijnberk LM, and Galli M (2024). Functional consequences of somatic polyploidy in development. Development 151, dev202392. 10.1242/dev.202392. [PubMed: 38415794]
34. Bestman JE, and Cline HT (2014). Morpholino Studies in Xenopus Brain Development. In Brain Development: Methods and Protocols, Sprecher SG, ed. (Humana Press), pp. 155–171. 10.1007/978-1-62703-655-9_11.
35. Bestman JE, Lee-Osbourne J, and Cline HT (2012). In vivo time-lapse imaging of cell proliferation and differentiation in the optic tectum of Xenopus laevis tadpoles. J. Comp. Neurol. 520, 401–433. 10.1002/cne.22795. [PubMed: 22113462]
36. Lanz MC, Zatulovskiy E, Swaffer MP, Zhang L, Ilerten I, Zhang S, You DS, Marinov G, McAlpine P, Elias JE, and Skotheim JM (2022). Increasing cell size remodels the proteome and promotes senescence. Mol. Cell 82, 3255–3269.e8. 10.1016/j.molcel.2022.07.017. [PubMed: 35987199]
37. Brown RL, Durbin J, and Evans JM (1975). Techniques for Testing the Constancy of Regression Relationships over Time. J. Roy. Stat. Soc. B 37, 149–163.
38. Schönenberger F, Deutzmann A, Ferrando-May E, and Merhof D (2015). Discrimination of cell cycle phases in PCNA-immunolabeled cells. BMC Bioinf. 16, 180. 10.1186/s12859-015-0618-9.
39. Leonhardt H, Rahn H-P, Weinzierl P, Sporbert A, Cremer T, Zink D, and Cardoso MC (2000). Dynamics of DNA Replication Factories in Living Cells. J. Cell Biol. 149, 271–280. [PubMed: 10769021]
40. Prigent C, and Dimitrov S (2003). Phosphorylation of serine 10 in histone H3, what for? J. Cell Sci. 116, 3677–3685. 10.1242/jcs.00735. [PubMed: 12917355]
41. Li DW, Yang Q, Chen JT, Zhou H, Liu RM, and Huang XT (2005). Dynamic distribution of Ser-10 phosphorylated histone H3 in cytoplasm of MCF-7 and CHO cells during mitosis. Cell Res. 15, 120–126. 10.1038/sj.cr.7290276. [PubMed: 15740641]
42. Fox MH (1980). A model for the computer analysis of synchronous DNA distributions obtained by flow cytometry. Cytometry 1, 71–77. 10.1002/cyto.990010114. [PubMed: 7023881]
43. Rosen LB, Ginty DD, Weber MJ, and Greenberg ME (1994). Membrane depolarization and calcium influx stimulate MEK and MAP kinase via activation of Ras. Neuron 12, 1207–1221. 10.1016/0896-6273(94)90438-3. [PubMed: 8011335]
44. Randlett O, Wee CL, Naumann EA, Nnaemeka O, Schoppik D, Fitzgerald JE, Portugues R, Lacoste AMB, Riegler C, Engert F, and Schier AF (2015). Whole-brain activity mapping onto a zebrafish brain atlas. Nat. Methods 12, 1039–1046. 10.1038/nmeth.3581. [PubMed: 26778924]
45. Thyme SB, Pieper LM, Li EH, Pandey S, Wang Y, Morris NS, Sha C, Choi JW, Herrera KJ, Soucy ER, et al. (2019). Phenotypic Landscape of Schizophrenia-Associated Genes Defines Candidates and Their Shared Functions. Cell 177, 478–491.e20. 10.1016/j.cell.2019.01.048. [PubMed: 30929901]
46. Sillar KT, and Li W-C (2020). Neural control of swimming in hatchling Xenopus frog tadpoles. In The Neural Control of Movement, Whelan PJ and Sharples SA, eds. (Academic Press), pp. 153–174. 10.1016/B978-0-12-816477-8.00007-7.
47. Saccomanno V, Love H, Sylvester A, and Li W-C (2021). The early development and physiology of Xenopus laevis tadpole lateral line system. J. Neurophysiol. 126, 1814–1830. 10.1152/jn.00618.2020. [PubMed: 34705593]
48. Roberts A, Li W-C, and Soffe SR (2010). How neurons generate behavior in a hatchling amphibian tadpole: An outline. Front. Behav. Neurosci. 4, 16. 10.3389/fnbeh.2010.00016. [PubMed: 20631854]
49. Jamieson D, and Roberts A (2000). Responses of young Xenopus laevis tadpoles to light dimming: possible roles for the pineal eye. J. Exp. Biol. 203, 1857–1867. 10.1242/jeb.203.12.1857. [PubMed: 10821743]
50. Walter T, and Couzin ID (2021). TRex, a fast multi-animal tracking system with markerless identification, and 2D estimation of posture and visual fields. eLife 10, e64000. 10.7554/eLife.64000. [PubMed: 33634789]
51. Vernon JA, and Butsch J (1957). Effect of tetraploidy on learning and retention in the salamander. Science 125, 1033–1034. 10.1126/science.125.3256.1033. [PubMed: 13432750]

Author Manuscript Author Manuscript Author Manuscript Author Manuscript

52. Fankhauser G, Vernon JA, Frank WH, and Slack WV (1955). Effect of Size and Number of Brain Cells on Learning in Larvae of the Salamander, Triturus viridescens. Science 122, 692–693. 10.1126/science.122.3172.692. [PubMed: 13255909]
53. Brown KM, Gillette TA, and Ascoli GA (2008). Quantifying neuronal size: summing up trees and splitting the branch difference. Semin. Cell Dev. Biol. 19, 485–493. 10.1016/j.semcdb.2008.08.005. [PubMed: 18771743]
54. Miller KE, and Suter DM (2018). An Integrated Cytoskeletal Model of Neurite Outgrowth. Front. Cell. Neurosci. 12, 447. 10.3389/fncel.2018.00447. [PubMed: 30534055]
55. Jakobs MAH, Franze K, and Zemel A (2020). Mechanical Regulation of Neurite Polarization and Growth: A Computational Study. Biophys. J. 118, 1914–1920. 10.1016/j.bpj.2020.02.031. [PubMed: 32229314]
56. Fan A, Tofangchi A, Kandel M, Popescu G, and Saif T (2017). Coupled circumferential and axial tension driven by actin and myosin influences in vivo axon diameter. Sci. Rep. 7, 14188. 10.1038/s41598-017-13830-1. [PubMed: 29079766]
57. Sengupta B, Faisal AA, Laughlin SB, and Niven JE (2013). The effect of cell size and channel density on neuronal information encoding and energy efficiency. J. Cereb. Blood Flow Metab. 33, 1465–1473. 10.1038/jcbfm.2013.103. [PubMed: 23778164]
58. Kolodkin AL, and Tessier-Lavigne M (2011). Mechanisms and Molecules of Neuronal Wiring: A Primer. Cold Spring Harb. Perspect. Biol. 3, a001727. 10.1101/cshperspect.a001727. [PubMed: 21123392]
59. Chowdhury D, Watters K, and Biederer T (2021). Synaptic recognition molecules in development and disease. Curr. Top. Dev. Biol. 142, 319–370. 10.1016/bs.ctdb.2020.12.009. [PubMed: 33706921]
60. Südhof TC (2021). The cell biology of synapse formation. J. Cell Biol. 220, e202103052. 10.1083/jcb.202103052. [PubMed: 34086051]
61. Cadart C, and Heald R (2022). Scaling of biosynthesis and metabolism with cell size. Mol. Biol. Cell 33, pe5. 10.1091/mbc.E21-12-0627.
62. Schmoller KM, and Skotheim JM (2015). The Biosynthetic Basis of Cell Size Control. Trends Cell Biol. 25, 793–802. 10.1016/j.tcb.2015.10.006. [PubMed: 26573465]
63. Fankhauser G (1945). Maintenance of normal structure in heteroploid salamander larvae, through compensation of changes in cell size by adjustment of cell number and cell shape. J. Exp. Zool. 100, 445–455. 10.1002/jez.1401000310. [PubMed: 21010861]
64. Harrison RG (1924). Some Unexpected Results of the Heteroplastic Transplantation of Limbs. Proc. Natl. Acad. Sci. USA 10, 69–74. 10.1073/pnas.10.2.69. [PubMed: 16576784]
65. Penzo-Méndez AI, and Stanger BZ (2015). Organ-Size Regulation in Mammals. Cold Spring Harb. Perspect. Biol. 7, a019240. 10.1101/cshperspect.a019240. [PubMed: 26187729]
66. Thorne RG, and Nicholson C (2006). In vivo diffusion analysis with quantum dots and dextrans predicts the width of brain extracellular space. Proc. Natl. Acad. Sci. USA 103, 5567–5572. 10.1073/pnas.0509425103. [PubMed: 16567637]
67. Kamali-Zare P, and Nicholson C (2013). Brain Extracellular Space: Geometry, Matrix and Physiological Importance. Basic Clin. Neurosci. 4, 282–286. [PubMed: 25337358]
68. Nicholson C, and Hrabětová S (2017). Brain Extracellular Space: The Final Frontier of Neuroscience. Biophys. J. 113, 2133–2142. 10.1016/j.bpj.2017.06.052. [PubMed: 28755756]
69. Faber DS, and Pereda AE (2011). Brain and Nervous System | Physiology of the Mauthner Cell: Function. In Encyclopedia of Fish Physiology, Farrell AP, ed. (Academic Press), pp. 73–79. 10.1016/B978-0-12-374553-8.00280-X.
70. Billings SM (1972). Development of the mauthner cell in Xenopus laevis: A light and electron microscopic study of the perikaryon. Z. Anat. Entwicklungsgesch. 136, 168–191. 10.1007/BF00519176. [PubMed: 4339562]
71. Denton RD, Greenwald KR, and Gibbs HL (2017). Locomotor endurance predicts differences in realized dispersal between sympatric sexual and unisexual salamanders. Funct. Ecol. 31, 915–926. 10.1111/1365-2435.12813.
72. Offner T, Daume D, Weiss L, Hassenklöver T, and Manzini I (2020). Whole-Brain Calcium Imaging in Larval Xenopus. Cold Spring Harb. Protoc. 2020. 10.1101/pdb.prot106815.

Author Manuscript Author Manuscript Author Manuscript Author Manuscript

73. Padovan-Merhar O, Nair GP, Biaesch AG, Mayer A, Scarfone S, Foley SW, Wu AR, Churchman LS, Singh A, and Raj A (2015). Single Mammalian Cells Compensate for Differences in Cellular Volume and DNA Copy Number through Independent Global Transcriptional Mechanisms. Mol. Cell 58, 339–352. 10.1016/j.molcel.2015.03.005. [PubMed: 25866248]
74. Voichek Y, Bar-Ziv R, and Barkai N (2016). Expression homeostasis during DNA replication. Science 351, 1087–1090. 10.1126/science.aad1162. [PubMed: 26941319]
75. Lessenger AT, Swaffer MP, Skotheim JM, and Feldman JL (2025). Somatic polyploidy supports biosynthesis and tissue function by increasing transcriptional output. J. Cell. Biol. 224, e202403154. 10.1083/jcb.202403154. [PubMed: 39652010]
76. Menon T, Borbora AS, Kumar R, and Nair S (2020). Dynamic optima in cell sizes during early development enable normal gastrulation in zebrafish embryos. Dev. Biol. 468, 26–40. 10.1016/j.ydbio.2020.09.002. [PubMed: 32937161]
77. Chen ZJ (2007). Genetic and Epigenetic Mechanisms for Gene Expression and Phenotypic Variation in Plant Polyploids. Annu. Rev. Plant Biol. 58, 377–406. 10.1146/annurev.arplant.58.032806.103835. [PubMed: 17280525]
78. Yu Z, Haberer G, Matthes M, Rattei T, Mayer KFX, Gierl A, and Torres-Ruiz RA (2010). Impact of natural genetic variation on the transcriptome of autotetraploid Arabidopsis thaliana. Proc. Natl. Acad. Sci. USA 107, 17809–17814. 10.1073/pnas.1000852107. [PubMed: 20876110]
79. Osborn TC, Pires JC, Birchler JA, Auger DL, Chen ZJ, Lee H-S, Comai L, Madlung A, Doerge RW, Colot V, and Martienssen RA (2003). Understanding mechanisms of novel gene expression in polyploids. Trends Genet. 19, 141–147. 10.1016/S0168-9525(03)00015-5. [PubMed: 12615008]
80. Guzowski JF, Timlin JA, Roysam B, McNaughton BL, Worley PF, and Barnes CA (2005). Mapping behaviorally relevant neural circuits with immediate-early gene expression. Curr. Opin. Neurobiol. 15, 599–606. 10.1016/j.conb.2005.08.018. [PubMed: 16150584]
81. Sakurai K (2024). Rethinking c-Fos for understanding drug action in the brain. J. Biochem. 175, 377–381. 10.1093/jb/mvad110. [PubMed: 38153290]
82. Kovács KJ (1998). Invited review c-Fos as a transcription factor: a stressful (re)view from a functional map. Neurochem. Int. 33, 287–297. 10.1016/S0197-0186(98)00023-0. [PubMed: 9840219]
83. Dulcis D, Lippi G, Stark CJ, Do LH, Berg DK, and Spitzer NC (2017). Neurotransmitter Switching Regulated by miRNAs Controls Changes in Social Preference. Neuron 95, 1319–1333.e5. 10.1016/j.neuron.2017.08.023. [PubMed: 28867550]
84. Thomas GM, and Huganir RL (2004). MAPK cascade signalling and synaptic plasticity. Nat. Rev. Neurosci. 5, 173–183. 10.1038/nrn1346. [PubMed: 14976517]
85. Hussain A, Saraiva LR, Ferrero DM, Ahuja G, Krishna VS, Liberles SD, and Korsching SI (2013). High-affinity olfactory receptor for the death-associated odor cadaverine. Proc. Natl. Acad. Sci. USA 110, 19579–19584. 10.1073/pnas.1318596110. [PubMed: 24218586]
86. Cancedda L, Putignano E, Impey S, Maffei L, Ratto GM, and Pizzorusso T (2003). Patterned vision causes CRE-mediated gene expression in the visual cortex through PKA and ERK. J. Neurosci. 23, 7012–7020. 10.1523/JNEUROSCI.23-18-07012.2003. [PubMed: 12904462]
87. Ji RR, Baba H, Brenner GJ, and Woolf CJ (1999). Nociceptive-specific activation of ERK in spinal neurons contributes to pain hypersensitivity. Nat. Neurosci. 2, 1114–1119. 10.1038/16040. [PubMed: 10570489]
88. Itoh M, Yamamoto T, Nakajima Y, and Hatta K (2014). Multistepped optogenetics connects neurons and behavior. Curr. Biol. 24, R1155–R1156. 10.1016/j.cub.2014.10.065. [PubMed: 25514003]
89. Dai Y, Iwata K, Fukuoka T, Kondo E, Tokunaga A, Yamanaka H, Tachibana T, Liu Y, and Noguchi K (2002). Phosphorylation of extracellular signal-regulated kinase in primary afferent neurons by noxious stimuli and its involvement in peripheral sensitization. J. Neurosci. 22, 7737–7745. 10.1523/JNEUROSCI.22-17-07737.2002. [PubMed: 12196597]
90. Li W-C (2021). Making In Situ Whole-Cell Patch-Clamp Recordings from Xenopus laevis Tadpole Neurons. Cold Spring Harb. Protoc. 2021. 10.1101/pdb.prot106856.

Author Manuscript Author Manuscript Author Manuscript Author Manuscript

91. Mawaribuchi S, Takahashi S, Wada M, Uno Y, Matsuda Y, Kondo M, Fukui A, Takamatsu N, Taira M, and Ito M (2017). Sex chromosome differentiation and the W- and Z-specific loci in Xenopus laevis. Dev. Biol. 426, 393–400. 10.1016/j.ydbio.2016.06.015. [PubMed: 27297884]
92. R Core Team (2013). R: A Language and Environment for Statistical Computing (Foundation for Statistical Computing).
93. Wickham H (2016). ggplot2: Elegant Graphics for Data Analysis (Springer International Publishing).
94. Wickham H, Averick M, Bryan J, Chang W, McGowan L, François R, Grolemund G, Hayes A, Henry L, Hester J, et al. (2019). Welcome to the Tidyverse. J. Open Source Softw. 4, 1686. 10.21105/joss.01686.
95. dplyr: A Grammar of Data Manipulation https://tidyverse.r-universe.dev/dplyr.
96. Kassambara A (2018). ggpubr:'ggplot2'based publication ready plots. R package version, 2.
97. Soneson C, Love MI, and Robinson MD (2015). Differential analyses for RNA-seq: transcript-level estimates improve gene-level inferences. F1000Res. 4, 1521. 10.12688/f1000research.7563.2. [PubMed: 26925227]
98. Love MI, Huber W, and Anders S (2014). Moderated estimation of fold change and dispersion for RNA-seq data with DESeq2. Genome Biol. 15, 550. 10.1186/s13059-014-0550-8. [PubMed: 25516281]
99. Schindelin J, Arganda-Carreras I, Frise E, Kaynig V, Longair M, Pietzsch T, Preibisch S, Rueden C, Saalfeld S, Schmid B, et al. (2012). Fiji: an open-source platform for biological-image analysis. Nat. Methods 9, 676–682. 10.1038/nmeth.2019. [PubMed: 22743772]
100. Ollion J, Cochennec J, Loll F, Escudé C, and Boudier T (2013). TANGO: a generic tool for high-throughput 3D image analysis for studying nuclear organization. Bioinformatics 29, 1840–1841. 10.1093/bioinformatics/btt276. [PubMed: 23681123]
101. Preibisch S, Saalfeld S, and Tomancak P (2009). Globally optimal stitching of tiled 3D microscopic image acquisitions. Bioinformatics 25, 1463–1465. 10.1093/bioinformatics/btp184. [PubMed: 19346324]
102. Arganda-Carreras I, Sorzano COS, Marabini R, Carazo JM, Ortiz-de-Solorzano C, and Kybic J (2006). Consistent and elastic registration of histological sections using vector-spline regularization. In Proceedings of the Second ECCV International Conference on Computer Vision Approaches to Medical Image Analysis CVAMIA'06, Beichel RR and Sonka M, eds. (Springer-Verlag), pp. 85–95. 10.1007/11889762_8.
103. Andrews S (2010). FastQC: a quality control tool for high throughput sequence data. https://github.com/s-andrews/FastQC.
104. Krueger F, James F, Ewels P, Afyounian E, and Schuster-Boeckler B (2021). FelixKrueger/TrimGalore: v0. 6.7-doi via zenodo. doi 10.5281/ZENODO.5127899.
105. Patro R, Duggal G, Love MI, Irizarry RA, and Kingsford C (2017). Salmon: fast and bias-aware quantification of transcript expression using dual-phase inference. Nat. Methods 14, 417–419. 10.1038/nmeth.4197. [PubMed: 28263959]
106. Stringer C, Wang T, Michaelos M, and Pachitariu M (2021). Cell-pose: a generalist algorithm for cellular segmentation. Nat. Methods 18, 100–106. 10.1038/s41592-020-01018-x. [PubMed: 33318659]
107. Nieuwkoop PD and Faber J, eds. (1994). Normal Table of Xenopus laevis (Daudin): A Systematical and Chronological Survey of the Development from the Fertilized Egg till the End of Metamorphosis (Garland Pub).
108. Affaticati P, Le Mével S, Jenett A, Rivière L, Machado E, Mughal BB, and Fini J-B (2018). X-FaCT: Xenopus-Fast Clearing Technique. Methods Mol. Biol. 1865, 233–241. 10.1007/978-1-4939-8784-9_16. [PubMed: 30151770]
109. Lopez V, Khakhalin AS, and Aizenman C (2021). Schooling in Xenopus laevis Tadpoles as a Way to Assess Their Neural Development. Cold Spring Harb. Protoc. 2021. 10.1101/pdb.prot106906.

Author Manuscript Author Manuscript Author Manuscript Author Manuscript

Highlights

- Triploid *Xenopus* displays a 1.5-fold increase in neuron volume compared with diploid
- Triploid neurons have longer neurites and increased cell surface area/volume ratio
- Triploid brains exhibit lower cell proliferation and higher neural activity
- Neuron size increase is associated with altered animal swimming behavior

Author Manuscript Author Manuscript Author Manuscript Author Manuscript

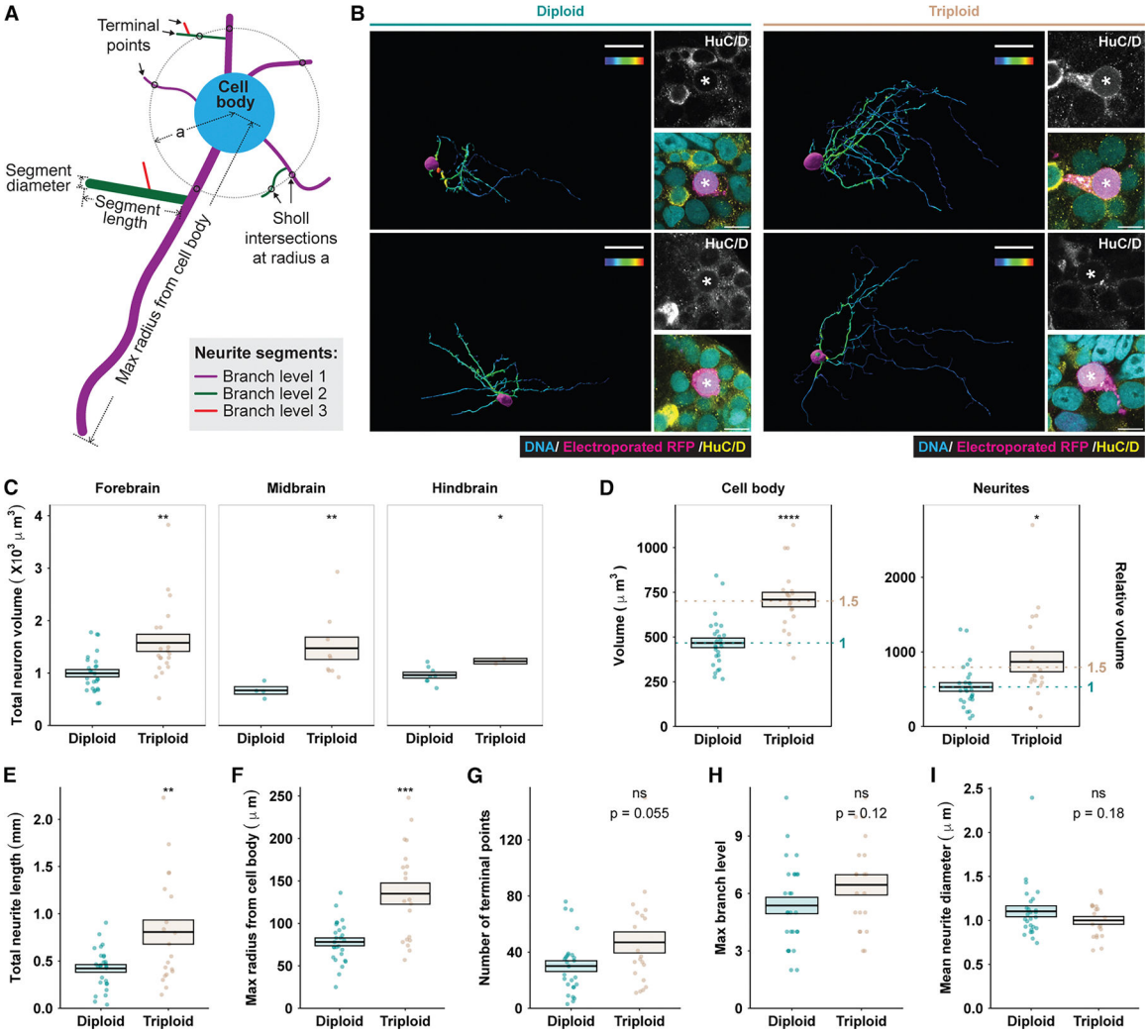


Figure 1. Triploid neurons are larger in volume and extend longer neurites

(A) Schematic showing different neuron size and shape parameters.

(B) Two representative examples of reconstructed electroporation-labeled diploid and triploid neurons with right images showing higher magnification micrographs of their cell bodies. The reconstructions were rotated to show the longest axes of the neurons and, therefore, cell bodies are not in the same orientation. Immunostaining of a pan-neuronal marker, the RNA-binding Hu proteins HuC/D (yellow), was used to confirm the neuronal identity of the labeled neurons[12] (magenta). Micrographs were taken at different laser settings, and their color channels were adjusted separately (see STAR Methods). In the reconstructions: scale bars, 30 μm; color bars, segment mean diameter 0–3 μm. In the zoomed-in micrographs: scale bars, 10 μm; asterisks, cell body of the labeled, reconstructed neuron. See also Figure S1 for details on the polyploid *Xenopus* model.

(C) Comparison of total neuron volume between diploid and triploid neurons. Numbers of diploid/triploid neurons measured were 26/17 in the forebrain, 4/8 in the midbrain, and 8/2 in the hindbrain. See also Figure S2A for Sholl analysis of these neurons.

(D) Comparison of cell body and neurite volume. Dotted lines, 1- and 1.5-fold of diploid mean.

Author Manuscript Author Manuscript Author Manuscript Author Manuscript

(E–I) Comparison of various size parameters: total neurite length (E), maximum radius from the cell body (F), number of terminal points (G), maximum branch level (H), and mean neurite diameter (I).

See also Figures S2B–S2H. Only forebrain neurons were used for analyses (D)–(I). In (C)–(I), each dot represents one neuron. Crossbars denote mean ± SEM. *$p < 0.05$, **$p < 0.01$, ***$p < 0.001$, and ****$p < 0.0001$; ns, not significant; *t* test.

Author Manuscript Author Manuscript Author Manuscript Author Manuscript

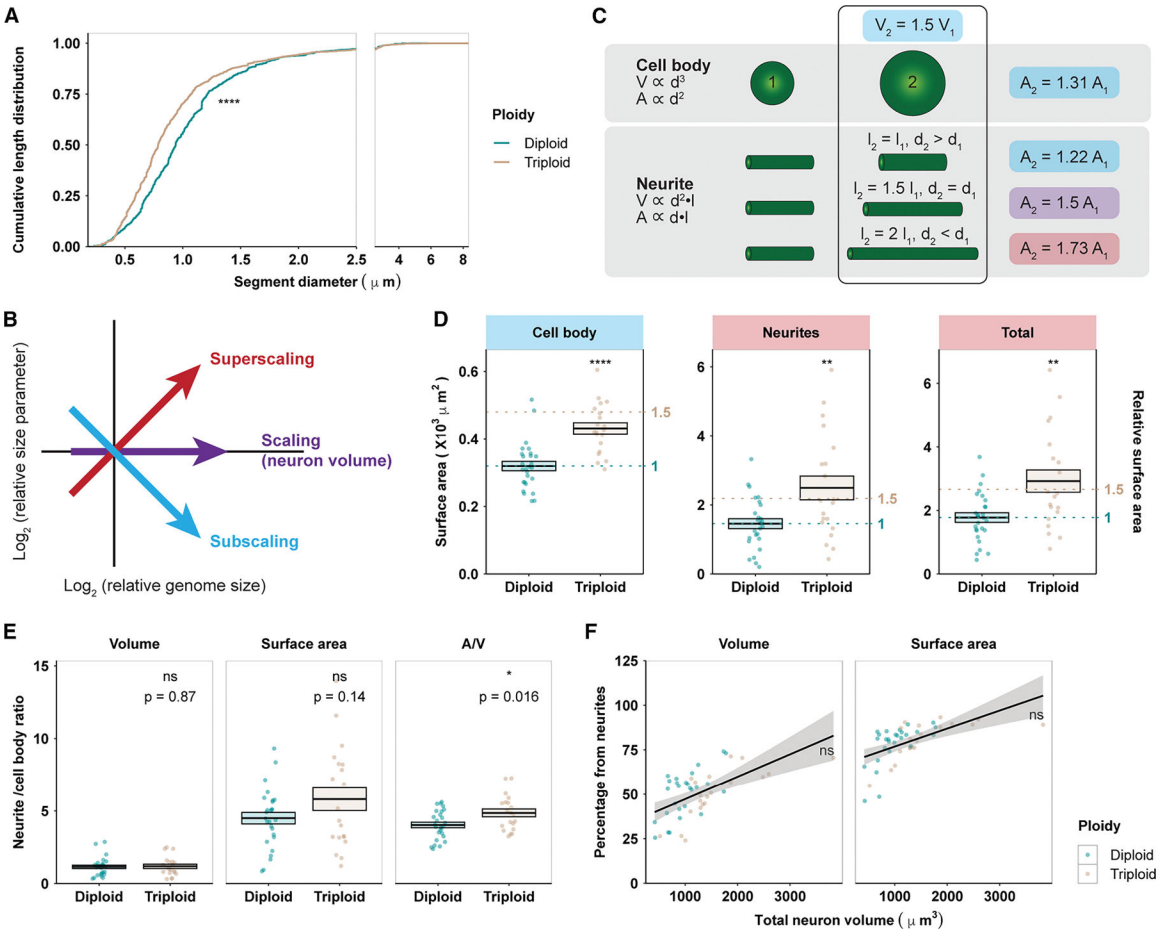


Figure 2. Cell surface area superscales with neuron ploidy and volume

(A) Cumulative length distribution of diploid and triploid neurites at different diameters. Leftward shift indicates a larger portion of neurite length with smaller diameter. ****$p <$ 0.0001, Kolmogorov-Smirnov test.

(B) Diagram defining different scaling relationships based on fold change differences. Inspired by Lanz et al.[36]

(C) Diagram modeling the differential increase in volume (V) and surface area (A) in relation to diameter (d) and length (l) in the cell body and neurites.

(D) Comparison of cell body, neurite, and total surface area between diploid and triploid neurons. Dotted lines, 1- and 1.5-fold of diploid mean.

(E) Ratios between the neurite and the cell body compartments for volume, surface area, and surface area/volume (A/V) in diploid and triploid neurons.

(F) Proportion of neuronal volume and surface area contributed by neurites. Diploid and triploid data were combined, smoothed with a linear model, and presented as the mean ± 95% confidence interval. ns, not significant, recursive CUSUM test.[37]

In (D)–(F), each dot represents one neuron. The same 26 diploid and 17 triploid forebrain neurons as in Figure 1 were analyzed. In (D) and (E), crossbars denote mean ± SEM. *$p <$ 0.05, **$p <$ 0.01, and ****$p <$ 0.0001; ns, not significant; *t* test.

Author Manuscript Author Manuscript Author Manuscript Author Manuscript

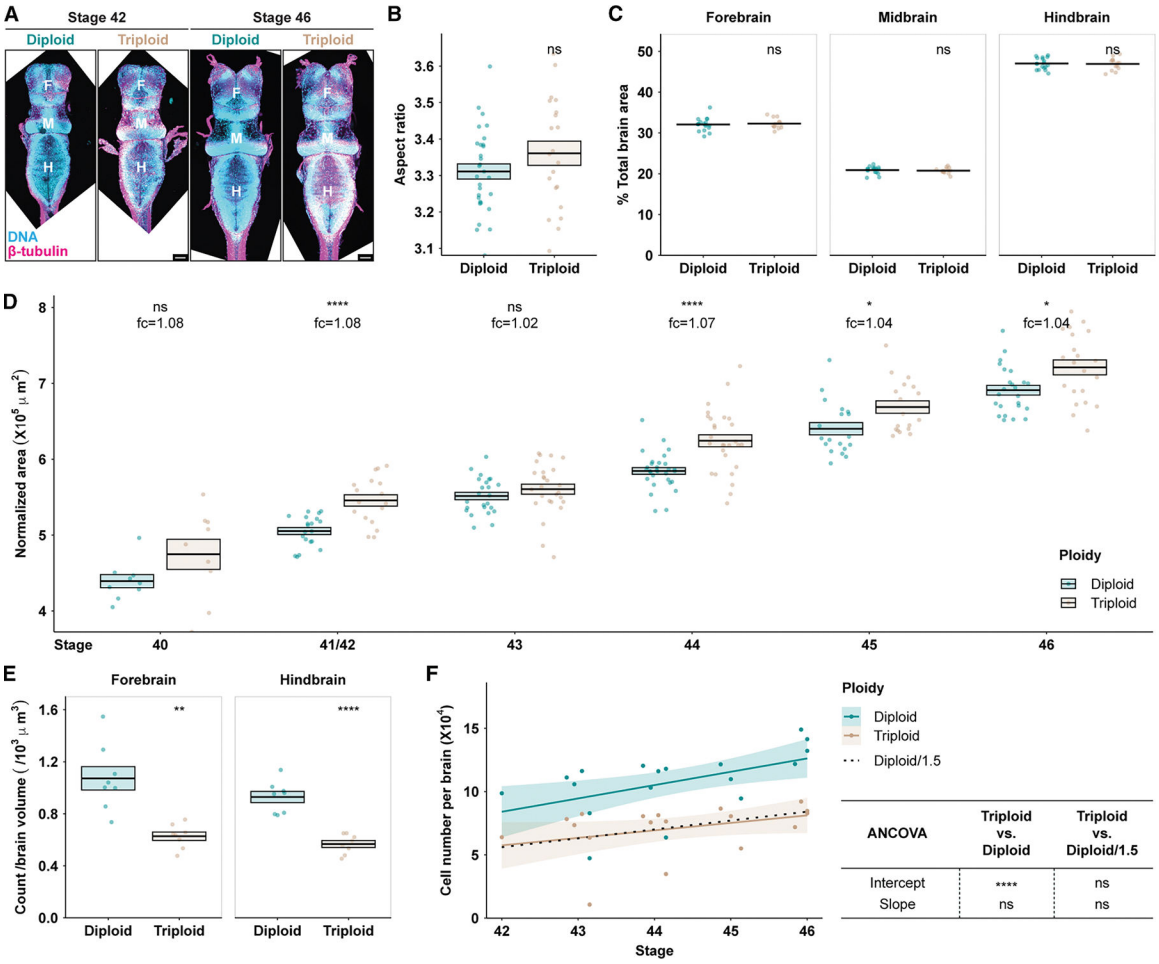


Figure 3. Triploid brains are morphologically similar to diploid brains but contain significantly fewer cells

(A) Representative *z*-projected micrographs of diploid and triploid brains at the indicated developmental stages. Stage 46 images were stitched from two overlapping tiles. F, forebrain; M, midbrain; H, hindbrain. Scale bars, 100 μm.

(B) Aspect ratio of diploid and triploid brains at stage 46. Each dot represents one brain and a total of 30 diploid and 21 triploid brains from four independent clutches were examined.

(C) Proportion of the indicated brain region in diploid and triploid brains at stage 46. A total of 18 diploid and 15 triploid brains from three independent clutches were examined. See also Figure S3A for data from different developmental stages.

(D) Size (area) comparison of diploid and triploid brains across multiple developmental stages. Numbers of diploid/triploid brains examined were 9/9 at stage 40, 20/17 at stage 41/42, 24/26 at stage 43, 30/28 at stage 44, 19/18 at stage 45, and 24/21 at stage 46. Brains were from four independent clutches. Areas were normalized to adjust for clutch variance. See also Figure S3B for brain area comparison in later-stage tadpoles, Figures S3C and S3D for brain height comparison, and Figures S3E and S3F for how sex did not impact brain size.

(E) Cell count normalized by volume in the indicated brain region in stage 46 diploid and triploid brains. Each dot represents imaging data from one brain. Eight brains per ploidy

Author Manuscript Author Manuscript Author Manuscript Author Manuscript

across three independent clutches were examined. Crossbars denote mean ± SEM. $^{**}p < 0.01$ and $^{****}p < 0.0001$; *t* test.

(F) Flow-cytometry-based estimates of cell count per brain in diploid and triploid brains across multiple developmental stages. Each dot represents one pooled sample of approximately six brains. Data were smoothed with a linear model and presented as the mean ± 95% confidence interval. The dotted "diploid/1.5" line is a regression of diploid data scaled by a factor of 1/1.5. $^{****}p < 0.0001$; ns, not significant; ANCOVA.

In (B)–(D), each dot represents one brain. Crossbars denote mean ± SEM. $^{*}p < 0.05$, $^{**}p < 0.01$, $^{***}p < 0.001$, and $^{****}p < 0.0001$; ns, not significant; *t* test. See also Figures S3G–S3I for similar metrics in *X. tropicalis*.

Author Manuscript Author Manuscript Author Manuscript Author Manuscript

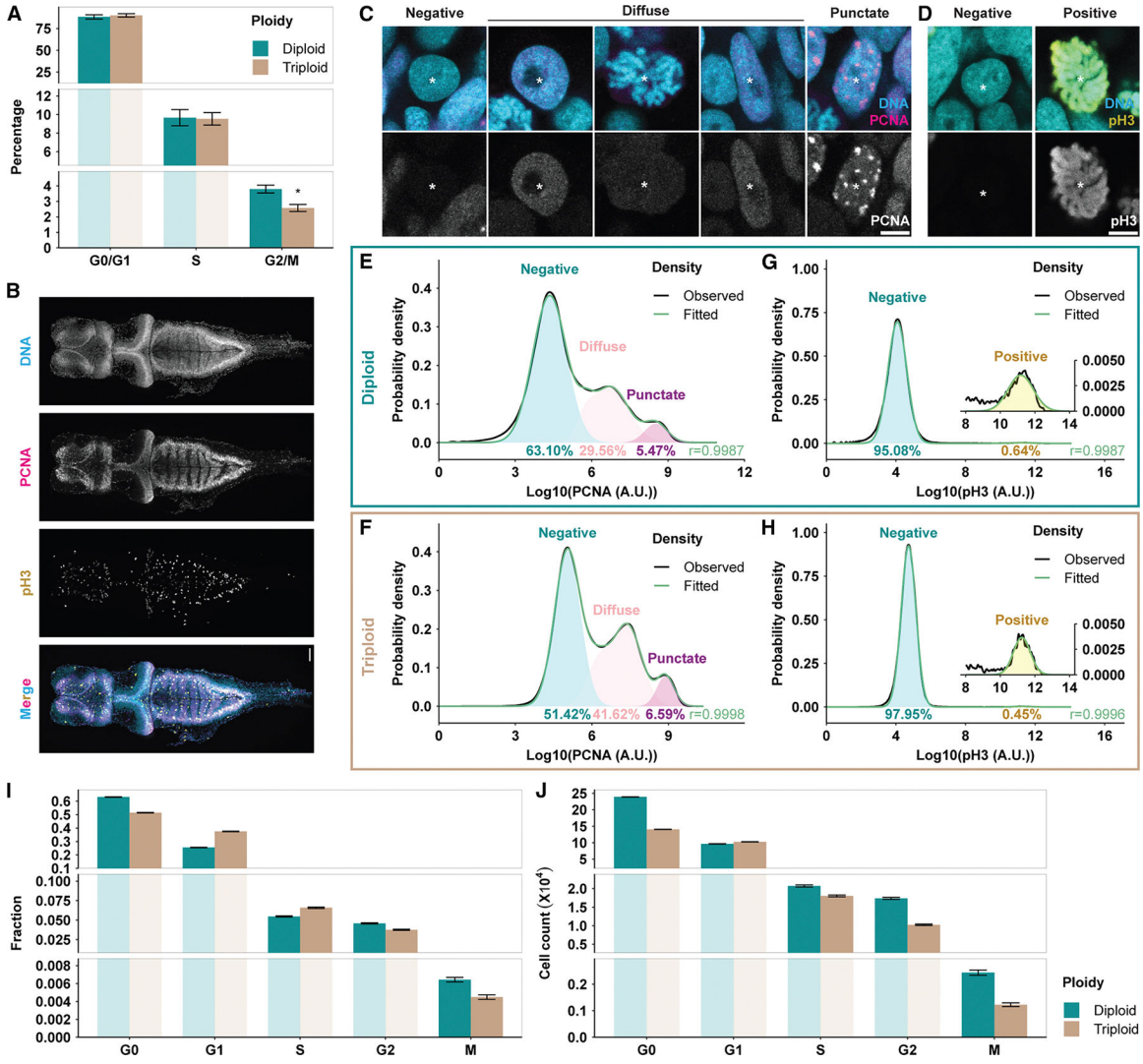


Figure 4. Triploid brains are less proliferative than diploid brains

(A) Cell-cycle analysis based on Hoechst intensity using the Dean Jett Fox (DJF) model.[42] Data were pooled from flow cytometry runs of five pairs of clutch-controlled diploid and triploid samples, each containing five or six developmental stage 46 brains. Mean ± SEM are shown. $*p < 0.05$, paired *t* test.

(B) Representative *z*-projected micrograph of a dissected stage 46 brain after co-staining with Hoechst and antibodies against PCNA and pH3, before dissociation for flow cytometry. Image was stitched from two overlapping tiles. Scale bar, 100 μm.

(C) Representative micrographs of three different PCNA expression patterns in the brain: (1) PCNA-negative (G_0) nuclei were all round-shaped, neuronal nuclei; (2) a diffuse PCNA pattern was observed in various nucleus shapes and phases, including round neuronal nuclei, elongated neural progenitor nuclei, and mitotic nuclei containing condensed chromosomes; (3) PCNA punctate (S) nuclei all possessed an elongated shape typical of progenitors. Asterisks, nuclei. Scale bar, 5 μm.

(D) Representative micrographs of two different pH3 expression patterns in the brain. Asterisks, nuclei of interest. Scale bar, 5 μm.

Author Manuscript Author Manuscript Author Manuscript Author Manuscript

(E and F) Probability density distribution of log10 PCNA level in representative diploid (E) and triploid (F) flow cytometry samples of dissociated brain cells at developmental stage 46. Gaussian distributions were used to fit the three populations as shown in (C). See also Figures S4A–S4C for DNA content distributions of the three PCNA populations.
(G and H) Probability density distribution of log10 pH3 level in representative diploid (G) and triploid (H) flow cytometry samples of dissociated brain cells at developmental stage 46. Gaussian distributions were used to fit the two populations as shown in (E). See also Figures S4D and S4E for DNA content distributions of the two pH3 populations.
(I and J) Comparison of fractions (I) and cell counts (J) of brain cell populations in different cell-cycle phases at developmental stage 46, calculated from six diploid and five triploid brains combining DNA content-based cell-cycle analysis (as in A) and PCNA/pH3 staining (as in E–H). Error bars mark 95% confidence interval.
See also Figure S4F for cell death data and Figure S5 for brain-specific RNA-seq data.

Author Manuscript Author Manuscript Author Manuscript Author Manuscript

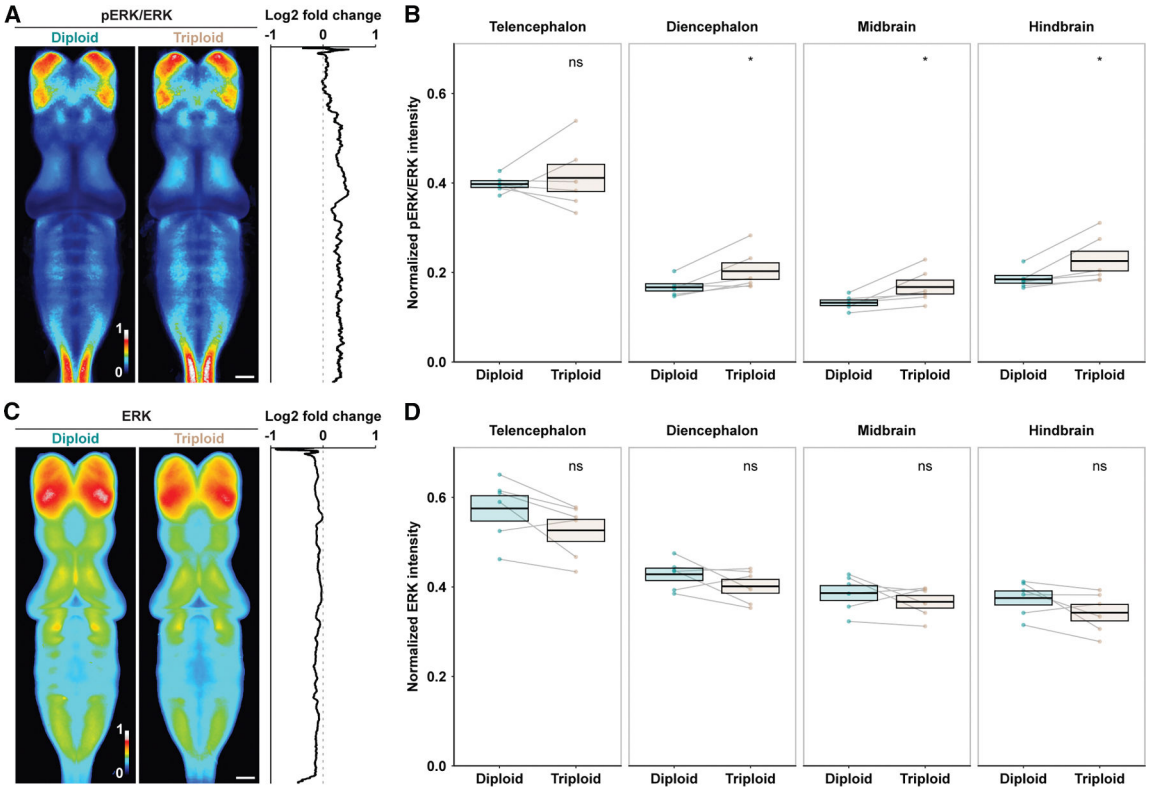


Figure 5. Triploid brains display changes in neural activity

(A) Heatmap showing normalized, averaged pERK/ERK intensity of 27 diploid and 26 triploid brains of unstimulated, freely swimming stage 46 tadpoles from six independent clutches. Log2 fold changes (triploid/diploid) of pERK/ERK intensity along the *y* axis are plotted to the right. Scale bar, 100 μm. See also Figure S6 for pERK expression patterns and response to stimuli.

(B) Comparison of pERK/ERK intensity in the indicated brain regions. Telencephalon and diencephalon make up the forebrain. Each dot represents the mean value of one clutch. Gray lines connect dots from the same clutch. Crossbars denote mean ± SEM. *$p < 0.05$; ns, not significant; paired *t* test.

(C) Heatmap showing normalized, averaged ERK intensity of the same brains as in (A). Log2 fold changes (triploid/diploid) of ERK intensity along the *y* axis are plotted to the right. Scale bar, 100 μm.

(D) Comparison of ERK intensity in the indicated brain regions. Each dot represents the mean value of one clutch. Gray lines connect dots from the same clutch. Crossbars denote mean ± SEM. ns, not significant; paired *t* test.

See also Figure S7A for RNA-seq and Figures S7B–S7D for RT-PCR examining ERK expression in the brain.

Author Manuscript Author Manuscript Author Manuscript Author Manuscript

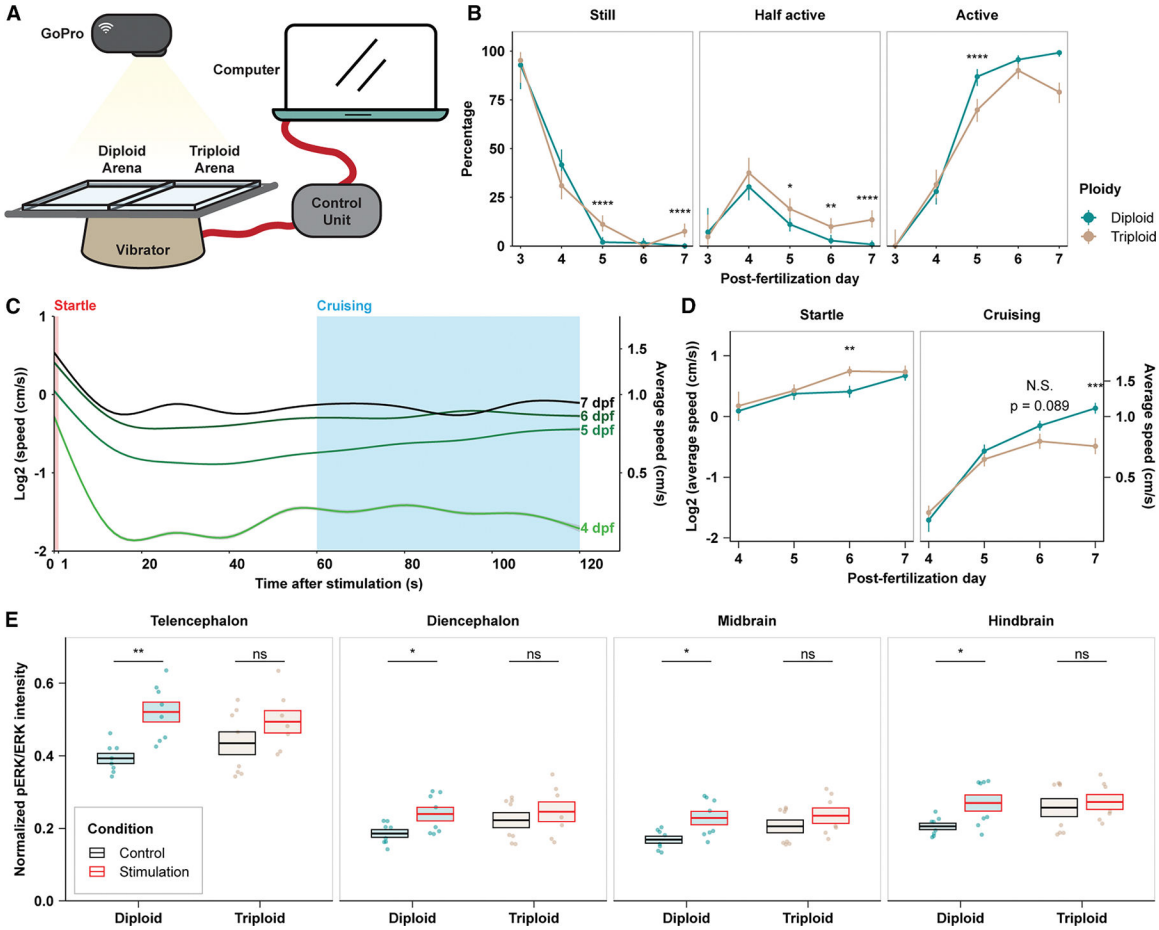


Figure 6. Neuron size and brain physiology differences produce distinct swimming behaviors in triploid tadpoles

(A) Diagram showing the experimental setup of the swimming assay. See also Figure S8A for the time scheme and Table S1 for the number of animals and replicates used.

(B) Manually scored categorization of the tadpoles based on their activity level. Error bars mark 95% confidence interval and data points are connected to show the trend over development. *$p < 0.05$, **$p < 0.01$, and ****$p < 0.0001$; Fisher's exact test. See also Figure S8B for the breakdown of the "half active" category.

(C) Real-time speed of TRex-tracked swimming tadpoles during the recorded 2-min window following stimulation. Diploid and triploid data were pooled. Data were smoothed with a generalized additive model (GAM) and presented as the geometric mean ± 95% confidence interval. Pink and blue boxes mark the time windows used to define the two different modes of swimming in (D).

(D) Comparison of diploid and triploid speeds under the indicated swimming mode. Data were log2 transformed to correct for non-normality and are presented as the geometric mean ± SEM. Each N represents one video. Numbers of N are reported in Table S2. **$p < 0.01$ and ***$p < 0.001$; *t* test.

(E) Comparison of pERK/ERK intensity in 6-dpf tadpole brains before and after repetitive vibrator stimulation. Telencephalon and diencephalon make up the forebrain. Each dot represents one brain. The numbers of brains examined were 8 for the diploid control group,

Author Manuscript Author Manuscript Author Manuscript Author Manuscript

8 for the diploid stimulation group, 8 for the triploid control group, and 7 for the triploid stimulation group. Brains were from two independent clutches. Crossbars denote mean ± SEM. *$p < 0.05$ and **$p < 0.01$; ns, not significant; *t* test. See also Figure S8C for heatmaps corresponding to these data and Table S2 for detailed statistical analysis.
See also Figure S8D for tadpole response after repetitive stimulation.

Author Manuscript Author Manuscript Author Manuscript Author Manuscript

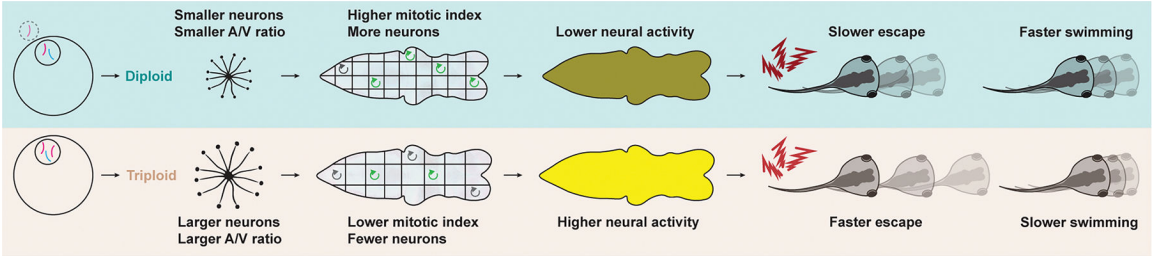


Figure 7. Schematic summary: ploidy and neuron size impact nervous system development and function in *Xenopus*

Author Manuscript Author Manuscript Author Manuscript Author Manuscript

KEY RESOURCES TABLE

REAGENT or RESOURCE	SOURCE	IDENTIFIER
Antibodies		
Mouse anti-HuC/HuD	Thermo Fisher Scientific	Cat#: A-21271; RRID: AB_221448
Mouse anti-β-tubulin	Developmental Studies Hybridoma Bank (DSHB)	Product name: E7 concentrate form; RRID: AB_2315513
Mouse anti-PCNA	Thermo Fisher Scientific	Cat#: 13–3900; RRID: AB_2533016
Mouse anti-p44/42 MAPK (Erk1/2)	Cell Signaling	Cat#: 4696
Rabbit anti-phospho-p44/42 MAPK (Erk1/2) (Thr202/Tyr204)	Cell Signaling	Cat#: 4370
Rabbit anti-phospho-Histone H3 (Ser10)	Millipore Sigma	Cat#: 06-570
Rabbit anti-RFP	Abcam	Cat#: ab62341
Rabbit anti-cleaved caspase-3 (Asp175)	Cell Signaling	Cat#: 9661
Alexa Fluor 488 goat anti-mouse IgG (H + L)	Thermo Fisher Scientific	Cat#: A-11001; RRID: AB_2534069
Alexa Fluor 568 goat anti-mouse IgG (H + L)	Thermo Fisher Scientific	Cat#: A-11004; RRID: AB_2534072
Alexa Fluor 488 goat anti-rabbit IgG (H + L)	Thermo Fisher Scientific	Cat#: A-11008; RRID: AB_143165
Alexa Fluor 568 goat anti-rabbit IgG (H + L)	Thermo Fisher Scientific	Cat#: A-11011; RRID: AB_143157
Bacterial and virus strains		
XL-1 Blue competent *Escherichia coli*	UC Berkeley QB3	N/A
Chemicals, peptides, and recombinant proteins		
Pregnant mare serum gonadotrophin	Calbiochem	Cat#: 367222
Human chorionic gonadotrophin	Sigma-Aldrich	Cat#: CG10
Hoechst 33342	Thermo Fisher Scientific	Cat#: H3570
Normal goat serum	Jackson ImmunoResearch	Cat#: 005-000-001; RRID: AB_2336983
StemPro Accutase	Thermo Fisher Scientific	Cat#: A1110501
Proteinase K	New England Biolabs	Cat#: P8107S
Paraformaldehyde (PFA) 16% Aqueous Solution EM Grade	Electron Microscopy Sciences	Cat#: 15710-S
CountBright Absolute Counting Beads	Thermo Fisher Scientific	Cat#: C36950
TRIzol Reagent	Invitrogen	Cat#: 15596026
DNase I	New England Biolabs	Cat#: M0303S
Critical commercial assays		
Phusion High-Fidelity PCR kit	New England Biolabs	Cat#: E0553S
Monarch RNA Cleanup Kit	New England Biolabs	Cat#: T2040S
iScript cDNA Sythesis Kit	Bio-Rad	Cat#: 1708890
iTaq Universal Probes Supermix	Bio-Rad	Cat#: 1725130
Experimental models: Organisms/strains		

Author Manuscript Author Manuscript Author Manuscript Author Manuscript

REAGENT or RESOURCE	SOURCE	IDENTIFIER
Xenopus laevis	Nasco	Cat#: LM00535
Xenopus laevis	National *Xenopus* Resource	Cat#: NXR_0031
Xenopus laevis (J strain)	National *Xenopus* Resource	Cat#: NXR_0024
Xenopus tropicalis	Nasco	Cat#: LM00822
Xenopus tropicalis	National *Xenopus* Resource	Cat#: NXR_1018
Oligonucleotides		
X. laevis W3 Forward: AAAACCATGACCTCCCGGATAC[91]	Integrated DNA Technologies	N/A
X. laevis W3 Reverse: TAGGGAGGGGTTTGGAGGTTC[91]	Integrated DNA Technologies	N/A
mapk1 Forward: *CTCATCCTTATCTGGAGCAGTATTAT*	Integrated DNA Technologies	N/A
mapk1 Reverse: *AGTGTCTCCTTGGGCAAATC*	Integrated DNA Technologies	N/A
mapk1 Probe: */56-FAM/ACCCAAGTG/ZEN/ ATGAGCCTGTAGCTG/3IABkFQ/*	Integrated DNA Technologies	N/A
gapdh Forward: *CAGCAGAGGGACCAATGAAA*	Integrated DNA Technologies	N/A
gapdh Reverse: *CGGCATCAAAGATGGAGGAATA*	Integrated DNA Technologies	N/A
gapdh Probe: */56-FAM/ACACACAAG/ZEN/ ACCAGGTTGTCTCCA/3IABkFQ/*	Integrated DNA Technologies	N/A
rpl8 Forward: *CAGGTCGTGCCTACCATAAAT*	Integrated DNA Technologies	N/A
rpl8 Reverse: *CCTGATGGTTGAGGGCTTAC*	Integrated DNA Technologies	N/A
rpl8 Probe: */56-FAM/TGGTGTGGC/ZEN/TATGAACCCTGTTGA/ 3IABkFQ/*	Integrated DNA Technologies	N/A
Recombinant DNA		
pCMV-GFP	Helen Willsey Lab, UCSF	N/A
Software and algorithms		
R (4.2.1), packages ggplot2, tidyverse, dplyr, ggpubr, Tximport, DESeq2	R core team[92]; Wickham[93]; Wickham et al.[94,95]; Kassambara et al.[96]; Soneson et al.[97]; Love et al.[98]	RRID: SCR_001905
ZEN 2.3 (Blue edition)	ZEISS	RRID: SCR_013672
FIJI, with plugins 3DSuite, Stitching	Schindelin et al.[99]; Ollion et al.[100]; Preibisch et al.[101]; Arganda-Carreras et al.[102]	RRID: SCR_002285
Imaris 10.2.0	Oxford Instruments Bitplane	RRID: SCR_007370
FlowJo 10.8.1	Becton Dickinson & Company	RRID: SCR_008520
fastQC	Andrews[103]	RRID: SCR_014583
Trim Galore	Krueger et al.[104]	RRID: SCR_011847
Salmon	Patro et al.[105]	RRID: SCR_017036
Cellpose	Stringer et al.[106]	RRID: SCR_021716
TRex	Walter and Couzin[50]	N/A
Other		
QB3 Genomics	UC Berkeley	RRID: SCR_022170

Author Manuscript

Author Manuscript

Author Manuscript

Author Manuscript

REAGENT or RESOURCE	SOURCE	IDENTIFIER
CRL Molecular Imaging Center	UC Berkeley	RRID: SCR_017852
CRL Flow Cytometry Facility	UC Berkeley	N/A